Research Square

Preprints are preliminary reports that have not undergone peer review.
They should not be considered conclusive, used to inform clinical practice,
or referenced by the media as validated information.

Differential Deformation and Retrogressive Evolution of the Linbang Landslide with Multiple Slip Surfaces under Reservoir Water-Level Fluctuations

Jibo Li
Chengdu University of Technology
Mingli Xie
xiemingli23@cdut.edu.cn
Chengdu University of Technology
Chaogang Li
Chengdu University of Technology
Shujun Ju
Chengdu University of Technology
Chaoyang He
Chengdu University of Technology
Jianhua Deng
PowerChina Zhongnan Engineering Corporation Limited

Research Article

Keywords: Reservoir water level fluctuation, Multiple slip surfaces, Differential deformation, Retrogressive evolution, Linbang landslide, SBAS-InSAR

Posted Date: November 13th, 2026

DOI: https://doi.org/10.21203/rs.3.rs-11462870/v1

License: This work is licensed under a Creative Commons Attribution 4.0 International License.
Read Full License

Additional Declarations: No competing interests reported.

Differential Deformation and Retrogressive Evolution of the Linbang Landslide with Multiple Slip Surfaces under Reservoir Water-Level Fluctuations

Jibo Li[1], Mingli Xie[1,2,3*], Chaogang Li[1], Shujun Ju[1,5], Chaoyang He[1,5], Jianhua Deng[4]

1 State Key Laboratory of Geohazard Prevention and Geoenvironment Protection, Chengdu University of Technology, Chengdu, Sichuan 610059, China;2 National Field Scientific Observation and Research Station of Geohazards in Badong, Wuhan, Hubei 430074, China;3 National Key Laboratory of Mountain River Protection and Governance,Sichuan University, Chengdu, Sichuan 610065, China;4 PowerChina Zhongnan Engineering Corporation Limited, Changsha 410014, China;5 State Power Dadu River Basin Hydropower Development Co., Ltd., Chengdu, Sichuan 610093, Chinae

E-mail: 1127191986@qq.com (Jibo Li)

*Corresponding author: Mingli Xie, e-mail:xiemingli23@cdut.edu.cn

Funding: This work was supported by the National Natural Science Foundation of China (Grant No. 42607301); the Open Fund of Badong National Observation and Research Station of Geohazards (Grant No. BNORSG-202406); and the Open Fund of State Key Laboratory of Hydraulics and Mountain River Engineering (Grant No. SKHL2422).

Abstract Fluctuations in reservoir water level are a major cause of the reactivation of ancient landslides along reservoir banks, yet for deposits controlled by weak intercalated zones, the differences in deformation response among individual sliding masses and the traction between them remain poorly understood. Taking the Linbang ancient landslide deposit in the Houziyan Reservoir of the Dadu River as a case study, this paper integrates SBAS-InSAR deformation identification, field monitoring, a large-scale physical model test and coupled seepage-stress numerical simulation to investigate the differential deformation of the sliding masses and the mechanism of traction-driven evolution under reservoir water level fluctuations. The results show that: (i) before impoundment, deformation was concentrated at the front edge and expanded towards the middle and rear parts after impoundment; the maximum cumulative displacement in the field reached 4674.94 mm, and accelerated deformation occurred mainly during the drawdown period from December to May, allowing the landslide to be divided into a strongly deformed front zone, a traction zone in the middle and a passively dragged zone at the rear. (ii) The physical model reproduced the initial impoundment and five subsequent water level cycles; seven cracks developed, and the maximum surface change obtained by 3D laser scanning increased from 2.75 cm in the first cycle to 3.68 cm in the fifth, with deformation propagating successively from J3 to J2 and J1, indicating retrogressive extension from the front towards the rear. (iii) Initial impoundment softened and settled the submerged sliding masses, weakening their support for the upper masses; during drawdown, internal drainage lagged behind the falling reservoir level, generating an outward seepage force superimposed on the downslope component, with pore pressure peaks lagging behind water level peaks; the strongly weathered phyllite-dominated mass, with high water retention and relatively slow drainage, is an important control on the stepwise deformation during drawdown. (iv) Numerical simulation further indicates that during water level rise the inward seepage force and external hydrostatic pressure provide a stabilizing contribution, whereas larger drawdown rates or higher rainfall intensities increase the reduction in stability. The deformation of the Linbang landslide is governed by traction between sliding masses, showing the staged characteristics of acceleration during initial impoundment, stepwise movement during drawdown and deceleration during the subsequent rise.

Keywords Reservoir water level fluctuation; Multiple slip surfaces; Differential deformation; Retrogressive evolution; Linbang landslide; SBAS-InSAR

Introduction

Fluctuations in reservoir water level alter the hydraulic boundary conditions of bank slopes, adjusting pore water pressure, seepage direction and stress state, and thereby influencing the reactivation and deformation of ancient landslides (Corbyn 1982; Fujita 1977; Schuster 1979). Weak structural layers have also been identified as a primary control on the failure path of large landslides in tectonic melange zones (Zhao et al. 2025). In deposits that have experienced multiple episodes of sliding, pre-existing slip surfaces and weak zones are commonly preserved, and the individual sliding masses that they control differ in position, structure and degree of exposure to water. Their deformation responses may therefore differ in magnitude, rate and onset time. Deformation of the submerged front further modifies the support conditions of the masses behind it, allowing deformation to propagate upslope. Understanding the evolution of such multiple-slip-surface landslides under reservoir water level fluctuations therefore requires simultaneous attention to the differential deformation of the individual masses and to the traction between them, and to how a local hydraulic disturbance drives progressive upslope deformation.

The deformation evolution of reservoir-bank landslides is governed jointly by geological structure and hydrodynamic processes. Geological structure determines the potential sliding paths and failure modes and provides the basis for interpreting the movement of different parts of a slope (Huang 2007). Reservoir fluctuations and rainfall influence reactivation by altering the hydraulic condition of the slope, and their effects need to be assessed together with slope structure (Huang et al. 2016; Iqbal et al. 2019; Kafle et al. 2022; Shen et al. 2018; Xia et al. 2020; Yang et al. 2021; Zou et al. 2021). Historical reservoir cases further show that impoundment and rapid reservoir-level change can trigger catastrophic slope failure (Jian et al. 2014). For unsaturated slopes, changes in matric suction

induced by rapid water level variation are also an important control on stability (Mao et al. 2020), while the buoyancy-induced weight loss during water level rise indicates that the mechanical effect of water level change is stage-dependent (Li et al. 2020). Physical model tests provide observational evidence for the deformation process under these effects: the graded, blockwise sliding of a landslide with a polyline-shaped sliding surface shows that, beyond overall displacement, the deformation of individual parts deserves attention (Pan et al. 2016), whereas studies of a pile-reinforced landslide under long-term reservoir operation extend the analysis to deformation evolution under sustained water level disturbance (Liu et al. 2020). These studies provide a basis for understanding structural control and hydraulic response, and they raise the key question for multiple-slip-surface landslides: how do the local responses of individual sliding masses produce differential deformation and, through mutual traction, drive deformation into adjacent areas?

Although these studies explain the hydraulic response and failure of reservoir-bank landslides, changes in overall displacement or in stability coefficients alone cannot fully capture the deformation linkage among sliding masses controlled by multiple slip surfaces. For such landslides, it is necessary to distinguish deformation caused directly by local hydraulic change from deformation caused by the movement of adjacent masses, and to explain how the two interact during evolution. Three questions arise: how do the individual sliding masses differ in their response to initial impoundment and to subsequent water level fluctuations; how does deformation of the front change the support conditions of the adjacent mass and propagate towards the middle and rear; and how do pore pressure lag, immersion-induced softening and seepage erosion affect this differential deformation and traction? Linking the sequence of movement, the displacement differences and the hydraulic and stress responses between masses is the key to explaining the traction-driven evolution of multiple-slip-surface landslides.

Time-series InSAR retrieves the spatial distribution and long-term variation of surface deformation, and thus provides a basis for identifying differences in deformation between parts of a landslide and for recognising the expansion of the deforming area. Combined with geological survey, surface displacement and borehole inclinometer records, it further helps to constrain the subdivision of the sliding masses and their structural relationships and to analyse the sequence of movement between them. Because surface deformation cannot by itself determine the activity of subsurface slip surfaces, physical model observations of crack development, mass displacement and hydraulic response are required in order to examine how local deformation is transferred to adjacent masses, while numerical simulation can analyse the seepage and stress adjustments caused by water level change and provide a mechanical basis for interpreting differential deformation and traction. Combining long-term deformation monitoring with process-based model analysis therefore helps to establish an explanation that links multiple-slip-surface structure, hydraulic response and deformation transfer between masses.

The Linbang ancient landslide deposit is located in the Houziyan Reservoir area of the Dadu River, where a strongly weathered phyllite gravelly soil weak zone is developed within the deposit and the front edge lies within the reservoir water level fluctuation zone. Field investigation and monitoring show that the front, middle and rear parts of the landslide differ in deformation, which expands from the front towards the middle and rear, providing a suitable case for studying differential deformation and traction-driven evolution controlled by multiple slip surfaces. Taking the Linbang landslide as the study object, this paper first identifies the deformation zoning, the time-series characteristics and their relationship with water level fluctuation by combining SBAS-InSAR, field investigation and ground monitoring data; it then establishes a large-scale physical model on the basis of a generalization of the slope structure, simulating initial impoundment and subsequent water level cycles, and analyses the sequence of movement of the individual masses, crack development and mutual traction using displacement, pore water pressure, earth pressure, water content, 3D laser scanning and image records; finally, numerical simulation under different water level variation rates and rainfall conditions is used to analyse how hydraulic response and stress adjustment affect deformation. The aim is to explain the causes of differential deformation among the masses under reservoir water level fluctuations, to clarify how local deformation at the front is transferred to the middle and rear through traction, and to reveal the mechanism of retrogressive evolution controlled by multiple slip surfaces, thereby providing a basis for interpreting deformation monitoring results and for identifying priority monitoring locations in composite reservoir-bank landslides.

Study area and deformation characteristics

Study area

The Linbang ancient landslide deposit is located on the right bank of the Dadu River in Kairao Village, Gezong Township, Danba County, 10 km from Danba County town and 37.5 km from the Houziyan Hydropower Station dam site, with its center at 102°1′17.11″ E and 30°43′15.69″ N. No Holocene active faults are distributed in the near field; neotectonic movement in the region is dominated by large-scale strong uplift, and the valleys are mostly deeply incised V-shaped gorges. The terrain is higher in the west and lower in the east, generally dipping toward the Dadu River, with a natural slope angle of 30–35°. The landslide is about 500 m long (elevation 1790–2100 m),

25–30 m thick, with a volume of 3.5–4.5 million m³. Its planform is an elongated, armchair-like tongue, with a clear boundary between the steep and gentle slopes against the rear mountain. The landslide body consists of gravelly soil of the Late Pleistocene landslide deposit layer (Q3del), brownish gray, dry to slightly wet, with a loose to slightly dense structure. The gravels are mainly dolomitic marble, schist and phyllite, angular, generally 2–15 cm in diameter and accounting for 55–60%, with silty soil and fine sand as filling. Inside the landslide body, a layer of gravelly soil dominated by strongly weathered phyllite forms a weak zone. The exposed bedrock is the Sinian Dengying Formation (Zbdn), a mixture of phyllite and schist with well-developed fissures in three main groups. The landslide front edge lies within the water level fluctuation zone of the reservoir, where reservoir water and pore water in the deposit recharge each other.

Comparison of optical remote sensing images acquired before and after impoundment (Fig. 1a, b) reveals a distinct accumulation body at the front edge, which is typical of an ancient landslide deposit. A field investigation in March 2024 found that deformation and failure had further intensified, distributed over the front, middle and rear parts of the slope: multiple lattice beams at the front were cracked and uplifted, more severely than in 2019; multiple cracks appeared on the village road at the front; the village road in the middle subsided; and sliding scratches were observed at the rear edge and side walls (Fig. 1c). These deformation signs indicate that the slope is dominated by settlement deformation.

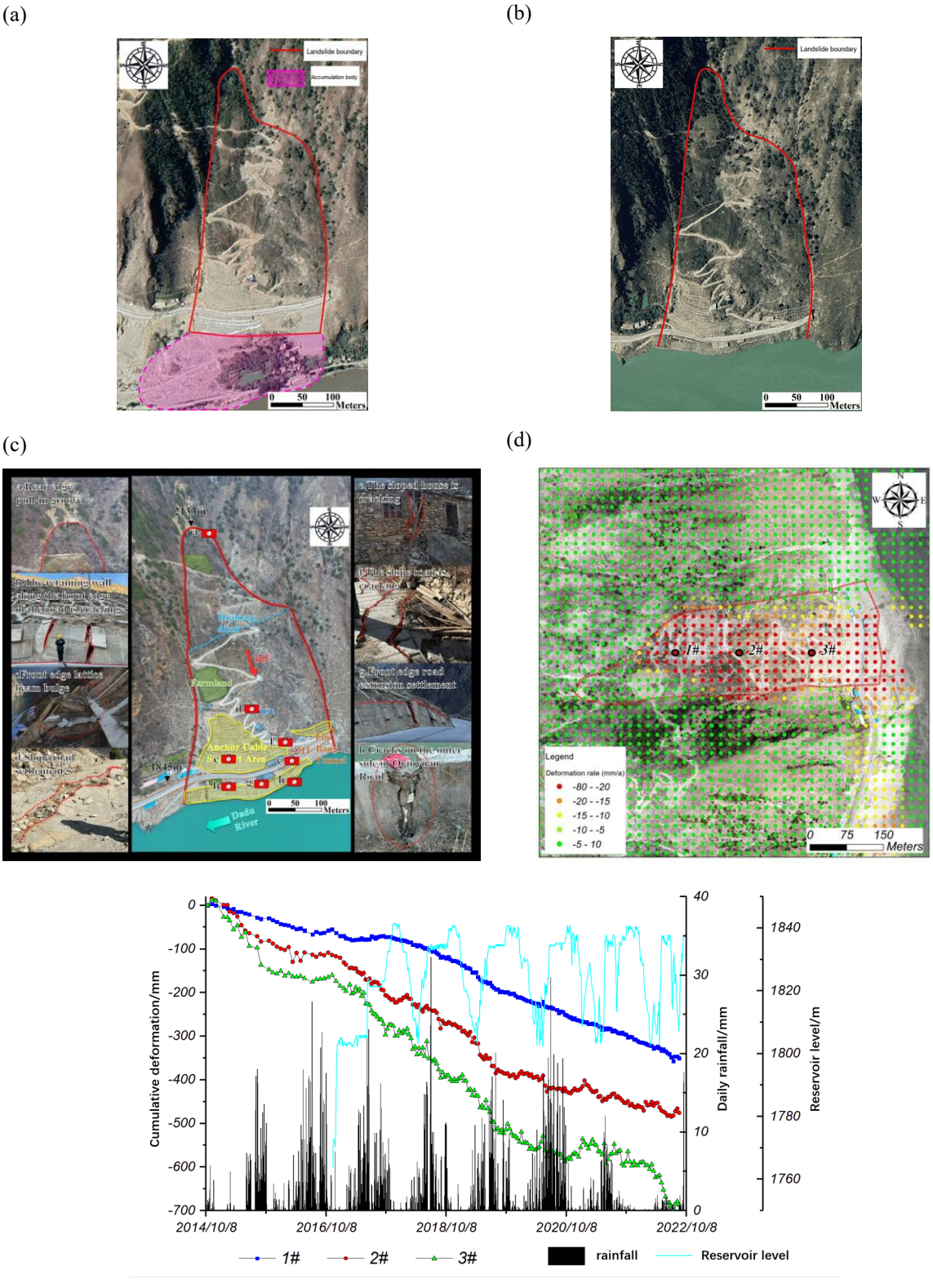


Fig. 1 Characteristics and deformation pattern of the Linbang landslide. (a,b) Optical remote-sensing images before and after impoundment; (c) panoramic view in 2024; (d) SBAS-InSAR displacement-rate map; (e) InSAR time-series displacement curves.

Deformation characteristics

Sliding masses and slip-surface structure

The Linbang ancient landslide has experienced multiple episodes of sliding, and the structure of the deposit preserves the characteristics of this multi-episode accumulation. According to the investigation, the source area consists, from top to bottom, of the Holocene colluvial layer (Q4cl+dl), the Late Pleistocene landslide deposit (Q3del) of gravelly soil, a lenticular intercalation of blocky soil within the lower part of the gravelly soil, which reflects the multi-episode accumulation of the ancient landslide, and the Sinian Dengying Formation (Zbdn) bedrock of phyllite, schist and dolomitic marble. Within the lower part of the gravelly soil, a layer dominated by strongly weathered phyllite is developed; it is highly weathered and its mechanical properties are markedly weakened, it occurs as a thick layer, and its maximum exposed thickness reaches 26 m, forming the weak intercalation of the slope.

According to this stratigraphic relationship, the Linbang landslide can be divided into three sliding masses, denoted masses 1, 2 and 3. Masses 1 and 3 consist of the gravelly soil of the Late Pleistocene landslide deposit, whereas mass 2 is the strongly weathered phyllite gravelly soil enclosed between them, that is, the weak intercalation of the slope. The three masses are therefore separated by the mass 1/2 and mass 2/3 interfaces which, together with the contact between the deposit and the bedrock, constitute several potential sliding horizons within the slope.

In this paper, the term multiple slip surfaces refers to these several potential sliding horizons within the composite deposit formed by multi-episode sliding, which are controlled by the weak intercalation and its upper and lower interfaces. Among them, the slip surface located near the deposit-bedrock contact and currently active is the main slip surface that controls the overall deformation of the landslide, its identification being based on the inclinometer monitoring results, while the remaining horizons are potential secondary slip surfaces. In the physical model test the slope was built in three episodes with three materials, so that the interfaces between the masses were preserved.

Analysis of the landslide deformation monitoring data

Based on 199 Sentinel-1 ascending-track scenes acquired between October 2014 and August 2022, the historical displacement field was retrieved by the SBAS-InSAR technique combined with a slope-aspect deformation separation algorithm. The displacement rate map (Fig. 1d) shows that before impoundment the deformation was mainly concentrated at the front edge, and that after impoundment it expanded progressively towards the middle and rear parts, forming a retrogressive progressive failure mode. The time-series displacement curves obtained from three monitoring points installed in the upper, middle and lower parts of the sliding mass (Fig. 1e) indicate that the reactivation process can be divided into three characteristic stages: an engineering-disturbance stage (before 2017), in which excavation of the road subgrade induced local reactivation at the front edge and the displacement rate decreased after anchor reinforcement; a hydraulic-driving stage (2017–2020), in which impoundment sharply increased the seepage pressure at the front edge and dragged the middle and rear parts into integral sliding along the bedrock contact; and a multi-stage sliding-surface development stage (after 2020), in which secondary sliding surfaces became gradually connected under the periodic fluctuation of the reservoir level and the tension-crack zone at the rear edge continued to expand.

In January 2017, 15 surface displacement observation piers and 6 borehole inclinometer systems were installed at the front edge of the sliding mass (Fig. 2a). The piers were arranged in three longitudinal monitoring sections along the main sliding direction, each with five equally spaced points, and were measured once a day with a total station. The three sections deform synchronously, showing an overall composite movement dominated by sliding towards the riverbed accompanied by vertical settlement; the deformation is largest in the central section 2#, smaller in section 1#, and decreases progressively from the front edge towards the rear. According to Table 1, the maximum cumulative deformation reaches 4674.94 mm (about 779 mm/a, point 2-3), whereas the rear section 3# deformed by only 294–376 mm (49–63 mm/a).

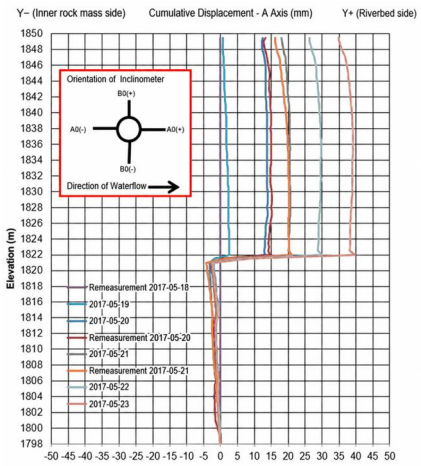
For deep-seated deformation monitoring, six borehole inclinometer holes (GX01-GX06) were installed at different elevations of the sliding mass in May-June 2017. Hole GX06 encountered a structural fracture of excessive width at a depth of 38 m, and the borehole was abandoned because the drill could not advance further; the remaining five holes failed within 7-15 days after installation, when the casings were structurally distorted by the severe deformation of the sliding mass. Despite the short effective monitoring period, the data obtained reveal key features of the deep-seated deformation: the displacement vectors of all holes are consistent in direction and point towards the free face and upstream, and the displacement-depth curves show a characteristic two-segment form, from which the slip surface was identified at about 28 m (GX01), 19 m (GX02), 33 m (GX03), 33.4 m (GX04) and 34 m (GX05); the slip surface therefore develops mainly within the weak intercalation in the lower part of the deposit and near its upper and lower interfaces. During the rapid rise of the reservoir water level on 14-16 June 2017, the measurement points at and above the slip surface in each hole accelerated markedly, indicating a direct response of slip-surface activity to water level change. According to the collar elevations of the holes, apart from hole GX03,

where the slip surface lies at about 1893 m and is therefore above the normal storage level, the slip-surface elevations of the remaining holes range from 1822 to 1840 m, that is, within the water level fluctuation zone of 1802-1842 m.

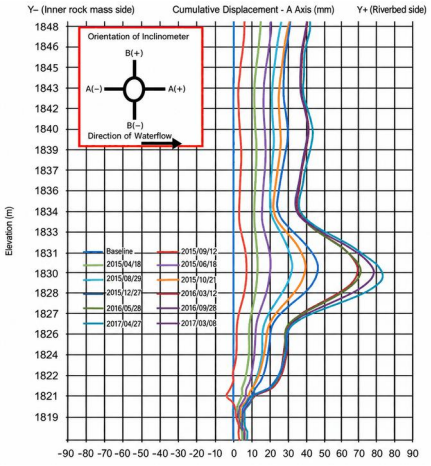
(a)



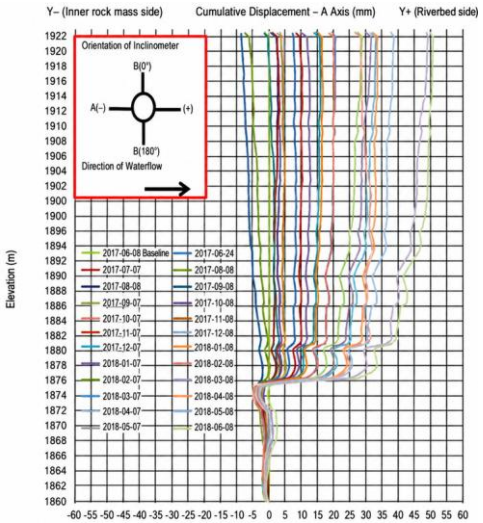
(b)



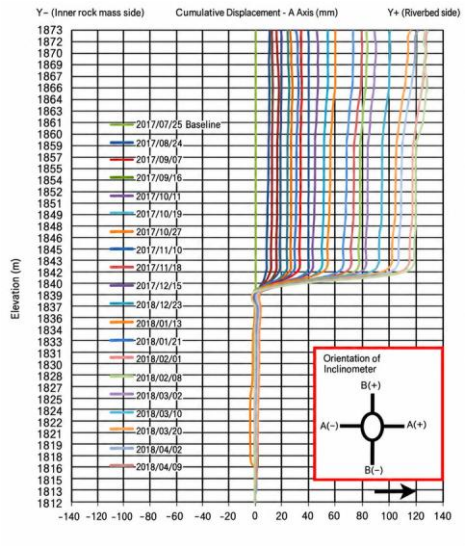
(c)



(d)



(e)



(f)

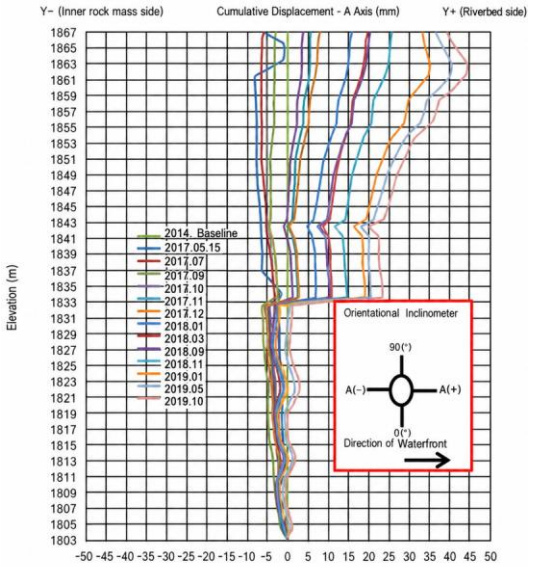


Fig. 2 Surface and borehole monitoring of the Linbang landslide. (a) Layout of surface displacement and inclinometer monitoring points; (b–f) displacement-depth curves for boreholes GX01–GX05.

Table 1 Statistics of the displacement monitoring data of the Linbang landslide

Section	Point	Time range	Cumulative displacement (mm)	Average annual displacement (mm)
	1-1	2017/3/2-2022/12/25	1694.91	282.48
	1-2	2017/3/2-2022/12/25	3571.07	595.17
1#	1-3	2017/3/2-2022/12/25	4204.56	700.76
	1-4	2017/3/2-2022/12/25	4188.58	698.09
	1-5	2017/3/2-2022/12/25	4470.74	745.12
	2-1	2017/3/2-2022/12/25	3963.78	660.63
	2-2	2017/3/2-2022/12/25	4458.89	743.14
2#	2-3	2017/3/2-2022/12/25	4674.94	779.15
	2-4	2017/3/2-2022/12/25	4653.70	775.61
	2-5	2017/3/2-2022/12/25	4440.88	740.14
	3-1	2017/3/2-2022/12/25	3127.74	521.29
	3-2	2017/3/2-2022/12/25	4167.01	694.50
3#	3-3	2017/3/2-2022/12/25	375.52	62.58
	3-4	2017/3/2-2022/12/25	293.91	48.98
	3-5	2017/3/2-2022/12/25	347.38	57.89

Based on the macroscopic characteristics of the monitoring curves (Fig. 3a,b), the deformation process of the Linbang landslide can be divided into three stages: (1) a severe deformation stage (January–June 2017), in which the front edge of the sliding mass deformed severely and the displacement vectors were highly consistent in direction, with an average daily displacement rate of 9.78 mm at point 2-5; (2) a deceleration stage (June 2017–April 2018), in which the deformation intensity was markedly weaker than in the first stage and was still largest at the front edge and decreased progressively towards the rear, with an average rate of 4.25 mm/d at point 2-5; and (3) a stepwise deformation stage (April 2018 to present), in which the deformation intensity was weaker than in the first two stages, again with larger deformation at the front edge and progressively smaller deformation at the rear, and an average rate of 1.25 mm/d at point 2-5. This stage shows obvious stepwise characteristics: the landslide accelerates markedly every year during the drawdown period (December–May).

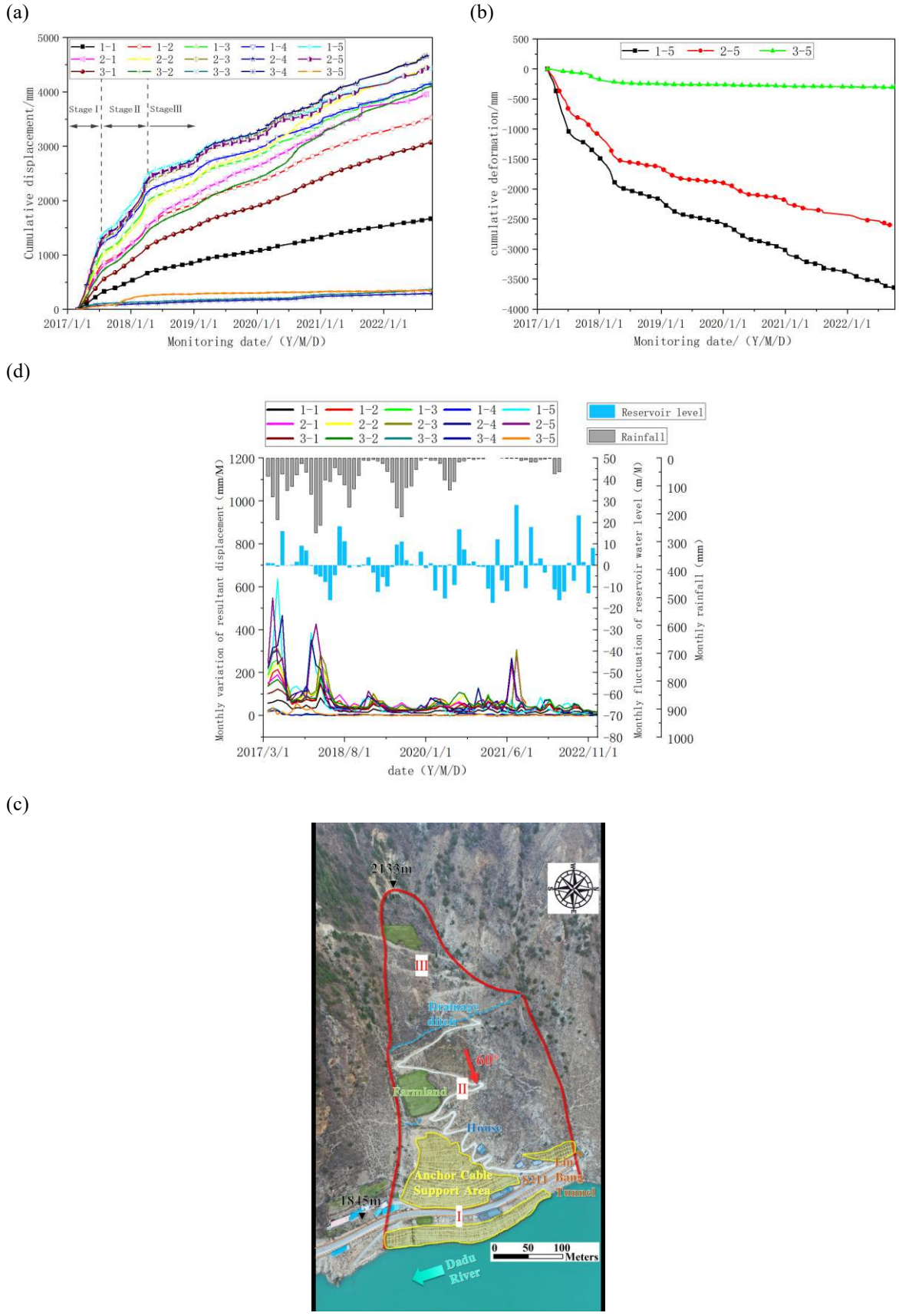


Fig. 3 Monitoring curves, deformation zoning and their relationships with reservoir and rainfall drivers. (a) Resultant displacement of the monitoring sections; (b) vertical displacement of front-edge stations in different sections; (c) deformation zoning; (d) monthly displacement, reservoir water level and rainfall.

According to the deformation signs and the analysis of the deformation monitoring data, the deformation of the landslide is controlled by the fluctuation of the reservoir water level: the closer the slope is to the reservoir water level, the more intense the deformation, showing a progressive retrogressive failure mode from the front towards the rear. The degree of deformation and failure at the front edge is greater than at the rear edge, and the landslide is divided into three zones according to the deformation degree (Fig. 3c). Zone I is mainly the anchor-cable support area at the front edge, which is most affected by the reservoir water level and deforms most strongly, and is classified as the strong deformation zone; Zone II is located in the middle of the sliding mass, is affected by the deformation of the front edge and connects with the rear part, and is classified as the traction zone; Zone III is located at the rear edge, has less deformation, and is deformed by the traction of Zone II, being classified as the passively dragged zone.

Analysis of the influencing factors of landslide deformation

Internal controlling factors

Topography and geomorphology: Deformation is concentrated near the slope toe, where the slope angle is 30°–35°. This terrain provides gravitational potential for slope movement without being so steep that collapse becomes the dominant form of deformation and reduces the potential energy of the slope mass. A pronounced scarp separates the landslide from the mountain behind it, concentrating tensile stress at the crest. The steep terrain also promotes shear stress concentration at the toe, where road excavation has created an additional scarp and substantially reduced slope stability. The Dadu River channel at the landslide front is wider than the reaches immediately upstream and downstream, providing an open free face that favours outward failure.

Material composition: The slope consists of colluvial gravelly soil with high porosity, poor cementation and high permeability. The landslide front lies within the reservoir water level fluctuation zone, where groundwater infiltration increases the self-weight of the slope and reduces soil cohesion, favouring sliding along the bedrock surface. The bedrock comprises phyllite and schist with well-developed, unfilled fractures. These fractures provide groundwater flow paths; water-induced softening of clay minerals in the phyllite and schist reduces the shear strength of discontinuities and threatens overall slope stability.

Slope structure: The landslide is approximately 25–30 m thick, and the natural slope angle at the toe is 30°–35°. It extends from an elevation of 1790.0 m to 2100.0 m, with a relief of 310.0 m. Its planform is an elongated, tongue-shaped, armchair-like outline, with a distinct transition from the steep mountain at the rear to the gentler landslide surface. Historical sliding striations are visible, the boundaries are relatively clear, and the constituent material is highly fragmented and weathered. A distinct accumulation body was present at the front before reservoir impoundment, identifying the slope as an ancient landslide deposit. Its considerable thickness, steep gradient and large relief provide substantial gravitational potential energy, while the open free face at the front allows outward movement. Within the landslide, a slightly dense layer of gravelly soil dominated by strongly weathered phyllite forms a weak zone that further reduces slope stability.

External controlling factors

The surface monitoring displacement data of the three sections (1#, 2# and 3#) of the Linbang landslide were correlated with the reservoir water level and rainfall monitoring data. The resultant displacement rates of the surface monitoring points were calculated, and their relationships with the rates of water level rise and drawdown and with the rainfall amount were analysed, as shown in Fig. 3d.

Reservoir water level rise and drawdown affect landslide deformation through different hydraulic processes. During a rise, groundwater recharge increases pore water pressure and may reduce effective stress and shear resistance, while inward seepage provides a stabilizing contribution. These effects act simultaneously. During drawdown, groundwater recession within the slope can lag behind the falling reservoir level, creating an outward hydraulic gradient. The resulting seepage force acts toward the free face and increases the downslope driving force, promoting deformation.

A comparison of the monthly variation of the resultant displacement with the monthly fluctuation of the reservoir water level shows that significant deformation occurred only during the first impoundment, when the water level rose; subsequent rises in the water level had only a limited effect on the slope. The second large fluctuation of the displacement curve corresponds to the first drawdown of the reservoir level, and the peak deformation rate occurred when the water level had fallen by half; thereafter, each drawdown stage was accompanied by a small fluctuation in the monthly resultant displacement curve. In the six months after 1 June 2021, the reservoir level underwent a cycle of drawdown–rise–drawdown, and the displacement was again noticeably disturbed. Overall, the rise of the reservoir water level has a weak influence on the deformation of this landslide, whereas the drawdown of the water level is the dominant factor inducing the deformation.

Rainfall infiltration can reduce slope stability by raising the groundwater level and pore water pressure, increasing the slope's self-weight and softening the soil and rock. However, the Linbang monitoring records show no consistent correspondence between displacement rate and the rainy season, nor between rainfall and the three pronounced peaks in displacement rate. The first two accelerations coincided with some rainfall, whereas rainfall was close to zero for several months around the third acceleration. Rainfall increased markedly in June–July 2019 without a corresponding increase in displacement rate. Daily rainfall was below 20 mm for most of the monitoring period, providing a relatively limited water supply to the slope. The well-developed pores in the upper gravelly soil allow infiltrating water to drain toward the slope toe through the soil and along the soil–bedrock contact, helping to limit sustained pore pressure buildup from rainfall. In contrast, the strongly deformed front lies within the reservoir fluctuation zone, where water level changes directly affect groundwater recharge and discharge. During drawdown, delayed groundwater recession produces outward seepage that promotes deformation of the front mass. Under the rainfall conditions observed during monitoring, rainfall-induced hydraulic disturbances were therefore relatively weak, while reservoir fluctuations and the associated groundwater adjustment exerted the main control on reactivation and deformation.

The maximal information coefficient (MIC) was used to quantify the association between displacement and the influencing factors (Table S1). The association was generally strongest for reservoir drawdown, followed by water level rise and rainfall. Values for drawdown reached 0.90 at point 2-5, with the points nearer the slope toe generally showing a stronger response to the changing reservoir boundary. Values for water level rise were approximately 0.6–0.7 at the main deforming points, whereas those for rainfall were generally below 0.3. At points 3-3, 3-4 and 3-5, the MIC values for all three factors did not exceed 0.55. These points also showed relatively small displacement, indicating a weaker deformation response to the monitored water level and rainfall variations.

Physical model test

Test design and procedure

Previous physical and geomechanical model tests have reproduced impoundment-induced deformation and failure of reservoir landslides (Du et al. 2018; Tang et al. 2018; Xiao et al. 2010). Taking the Linbang landslide, a typical accumulation landslide in the Dadu River basin, as the research object, a physical model test was conducted to investigate the deformation and failure behaviour of the landslide under reservoir impoundment. Based on the test objectives, methods and constraints, the prototype was scientifically generalized, including the modeling reconstruction of geological structural characteristics and environmental factors. Geological layering was simulated based on the selected section: complex strata were simplified into characteristic engineering geological units through the zoning of geotechnical materials, and the generalized model is shown in Fig. 4. The model strictly followed the geometric similarity criterion. According to the characteristic parameters of the prototype landslide (vertical height H = 230 m, horizontal extension L = 400 m) and the bearing capacity of the test system, the geometric similarity ratio was determined to be 1:200. The final model measures 200 cm × 100 cm × 115 cm (length × width × height). The actual height difference between the normal storage level and the pre-impoundment level is 40 m, corresponding to 20 cm in the model.

Before the model test, the physical and mechanical properties of the three sliding masses were determined by laboratory tests on samples taken from the site. Grain-size analysis indicated that sliding masses 1 and 3 consist of gravelly soil with a similar gradation and a low fine-particle content, whereas sliding mass 2 is dominated by strongly weathered phyllite with a markedly higher fine-particle content. Medium-scale direct shear tests performed on natural and saturated samples showed that saturation strongly reduces the cohesion of the gravelly soils (from 2.1–2.2 kPa to 0.1–0.2 kPa) and slightly reduces their friction angle (from 34.2°–35.1° to 30.7°–31.6°), while the phyllite-dominated soil has a higher cohesion (16.3 kPa) but a lower friction angle (26.7°), which decrease to 14.3 kPa and 25.7° when saturated. Laboratory permeability tests showed that the strongly weathered phyllite soil retains water much more strongly than the adjacent gravelly soils. Because the strength parameters and the permeability govern the water-level-driven deformation, they were adopted as the key similarity variables: the model soils were prepared by adjusting the compaction effort until the friction angle (34.5° for sliding masses 1 and 3 and 26.4° for sliding mass 2) and the permeability satisfied the similarity relations for a geometric ratio of 1:200.

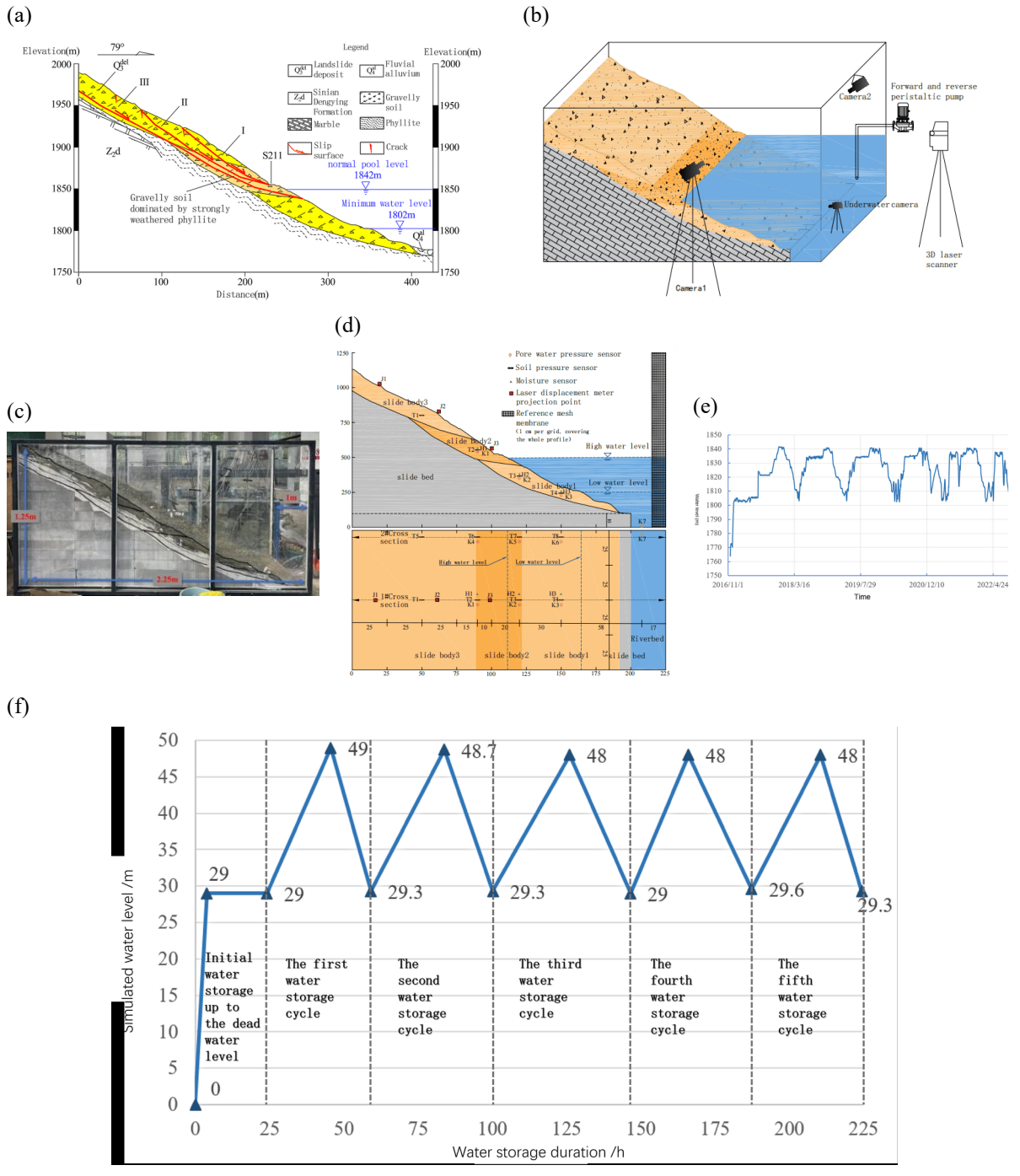


Fig. 4 Physical model design and impoundment scheme. (a) Geological section of the strongly deformed area; (b) generalized model; (c) model-box dimensions; (d) monitoring-point layout; (e) reservoir water-level variations; (f) simulated impoundment process.

The test used a model box measuring 2.5 m × 1 m × 1.25 m (length × width × height) (Fig. 4c). Earth pressure sensors, pore water pressure sensors and water content sensors were connected to a computer through a data acquisition instrument, and the monitoring data were collected and stored in real time, providing full-time curves of earth pressure, pore water pressure and water content, as well as digital image data of the landslide evolution process.

To investigate the evolution of the stress, seepage and displacement fields of the Linbang landslide under reservoir impoundment, a multi-source data fusion monitoring system was established, focusing on soil water content, pore water pressure, earth pressure and surface deformation. The system integrates earth pressure sensors, pore water pressure sensors, water content sensors, laser displacement meters, a 3D laser scanner and a multi-view camera

system (including front-view, side-view and underwater cameras), with sensor arrays embedded inside the slope. The spatial layout of the monitoring devices is shown in Fig. 4d.

The water level variation in the Houziyan Reservoir area from the start of impoundment on 17 November 2016 to 15 August 2022 was physically simulated in the test. The actual impoundment lasted 2098 days (50,352 h), corresponding to a simulated test duration of 224.4 h according to the time similarity ratio. As shown in Fig. 4e, the reservoir water level has fluctuated periodically between 1802 m and 1842 m since the operation of the hydropower station. Because the water level varies considerably within each cycle, the minimum and maximum levels of each cycle were selected for simulation, and the fluctuations within each cycle were simplified as uniform rise and decline. The corresponding minimum and maximum water levels in the model are 29.00 cm and 49.00 cm. The simulation was divided into six stages: the initial impoundment to the dead water level and five subsequent storage cycles (Fig. 4f).

The experimental procedure was as follows:

(1) After the model was built, it was left to stand for two days with a small amount of water mist sprayed to maintain soil moisture. Data acquisition of earth pressure, pore water pressure, water content and laser displacement was then started and continued until the end of the test, and the first 3D laser scanning was performed.

(2) The first impoundment was conducted: the water level was raised to the actual low level of 1802 m (29 cm in the model) and held for 20.19 h, followed by the second 3D laser scanning.

(3) The first water level fluctuation cycle was carried out at the designed rate and duration, followed by another 3D laser scanning. One rise–decline cycle is defined as one storage cycle, and a 3D laser scan was performed after each of the five cycles.

(4) After the fifth cycle, data acquisition was stopped and all data were exported for analysis.

Test results

Macroscopic deformation analysis

Stage 1 (severe deformation stage) includes the initial impoundment to the dead water level and the first storage cycle. During the water level rise, four cracks developed in the model: cracks 1–3 mainly occurred in the upper part of the slope (sliding mass 3), while crack 4 was located at the boundary between sliding masses 3 and 2 (Fig. 5a). Crack 1, at the top of the slope, showed obvious subsidence with a step-like morphology and was the longest crack at this stage; crack 4 extended into the slope interior. During the drawdown phase of the first storage cycle, deformation continued (Fig. 5b): the subsidence of crack 1 intensified by 0.5 cm; cracks 2 and 3 coalesced into a crack nearly traversing the entire model, 83.2 cm long and 2.9 cm deep, with a step height of 3.2 cm; crack 4 expanded by 3.1 cm in length, 0.4 cm in width and 0.3 cm in depth, with many secondary cracks developing around it.

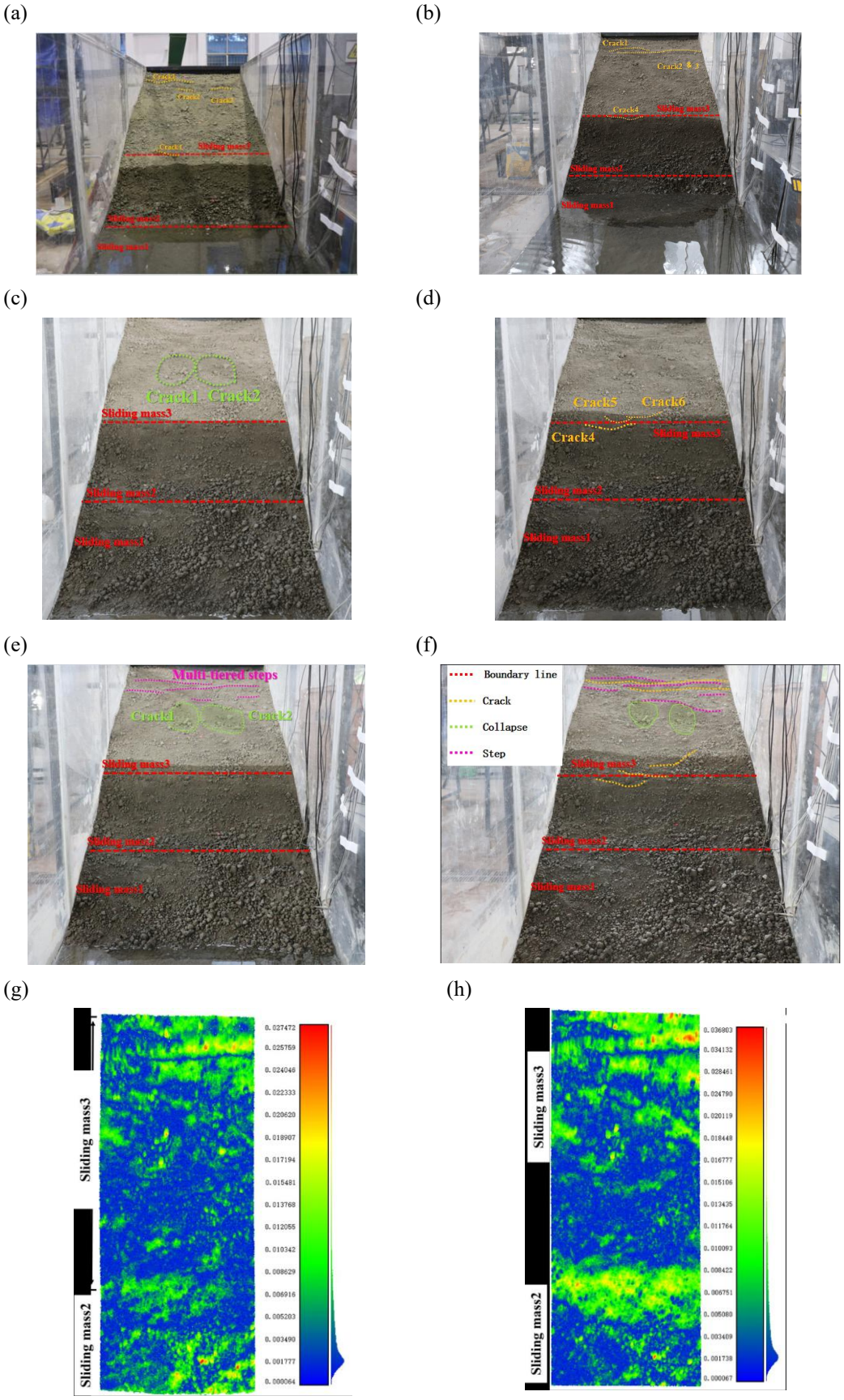


Fig. 5 Macroscopic and differential deformation in the physical model. (a,b) Stage 1 deformation during water-level rise and drawdown; (c–f) Stage 2 deformation after the second to fifth storage cycles; (g,h) 3D laser-scanning differential deformation after Stage 1 and after five cycles.

Stage 2 (deceleration stage) covers the second to fifth storage cycles, with deformation much smaller than in Stage 1. At the end of the second cycle, two new collapses appeared below cracks 2 and 3, with collapse 2 larger than collapse 1 (Fig. 5a). At the end of the third cycle, the secondary cracks between sliding masses 2 and 3 expanded into new cracks 5 and 6 (Fig. 5b). At the end of the fourth cycle, multi-level steps appeared in the upper part of sliding mass 3 (Fig. 5c), with a maximum vertical drop of 4.5 cm, while collapses 1 and 2 further intensified, showing a downward sliding trend. At the end of the fifth cycle, a new secondary crack developed along crack 1 and connected with it, causing crack 1 to traverse the entire slope, though much smaller in scale (Fig. 5d).

In total, seven cracks developed after five storage cycles: cracks 1, 2, 3 and secondary cracks with multi-level steps in the upper slope; two collapses in the upper-middle part; and cracks 4, 5 and 6 in the middle. Crack 1 and the secondary crack connected to traverse the whole slope, and cracks 2 and 3 merged into one crack in the later stage.

To quantify the deformation, the 3D laser scanning data were compared by differencing in two stages: the scan after the first storage cycle was differenced with the pre-impoundment scan to obtain the Stage 1 deformation map (Fig. 5g), and the scan after the fifth cycle was differenced with the pre-impoundment scan to obtain the final deformation map (Fig. 5h). After the first cycle, deformation was concentrated in the lower part of sliding mass 2 and the upper part of sliding mass 3, with a maximum of 2.75 cm; after the fifth cycle, deformation in the upper part of sliding mass 3 increased to a maximum of 3.68 cm, the largest on the slope, while deformation at the boundary between sliding masses 2 and 3 expanded significantly in a banded pattern, with a maximum of 3.4 cm.

Combining the high-definition images and 3D laser scanning data, after the first impoundment, both sliding masses 2 and 3 deformed significantly: sliding mass 2, located in the water level fluctuation zone with finer and well-graded particles, underwent overall settlement after softening by reservoir water immersion, and cracks developed between it and sliding mass 3; sliding mass 3 lost support due to the deformation of sliding mass 2 below, producing significant displacement and multi-level cracks in its upper part. The maximum deformation during this first storage cycle reached 2.45 cm.

In Stage 2, deformation slowed down overall, with only new secondary cracks and no large-scale new cracks; the cumulative deformation over four storage cycles was only 0.93 cm. Since sliding mass 2 lies in the fluctuation zone, its internal seepage field and earth pressure field change in every storage cycle, so deformation accumulates continuously but at a decreasing rate, indicating that the landslide was in a severe deformation stage during the first impoundment and gradually stabilized afterwards, showing a self-adaptive behaviour.

The model and field records share the broad pattern of pronounced deformation during initial impoundment followed by slower deformation in later cycles. Their stage-by-stage correspondence is examined below using the monitoring records.

Monitoring data analysis

(1) Earth pressure

The earth pressure data for the whole test process are plotted in Fig. 6a, where T1–T4 are located in monitoring section 1 and T5–T8 in section 2. The curves show strong synchronization between points at the same elevation in different sections. Points T2, T3, T4 and T6, T7, T8 are located at or below the highest water level and are greatly affected by reservoir fluctuations; after the first storage cycle, their curves show a positive correlation with the water level. In contrast, T1 and T5 at the top of the slope, far from the highest water level, show a continuous decreasing trend.

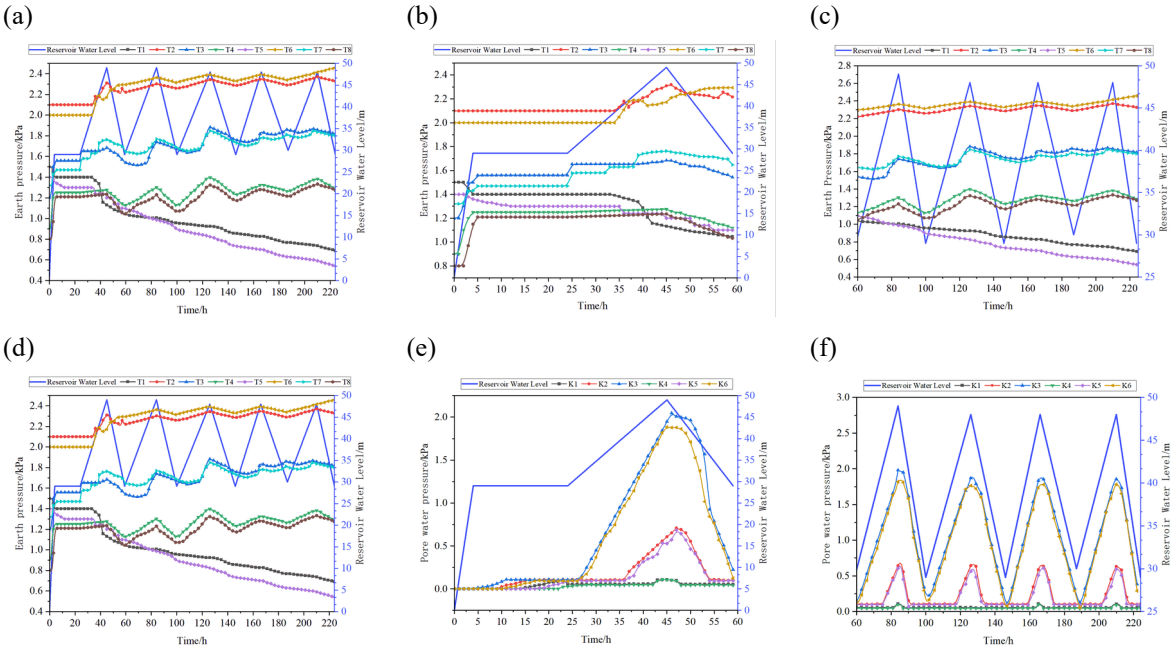


Fig. 6 Pressure response of the physical model. (a–c) Earth-pressure curves for the whole test, Stage 1 and Stage 2, respectively; (d–f) pore-water pressure curves for the whole test, Stage 1 and Stage 2, respectively.

In Stage 1, during the first 5 hours, as the water level rose to the dead water level, T4 and T8 increased significantly because they lie below the dead water level: reservoir water infiltrated the slope, increasing the unit weight of the overlying soil. As the water level rose further, T3 and T7, then T2 and T6, increased successively. Field observations show that although the water level had not reached the sensor elevations, rising groundwater transported water upward through capillary action, causing settlement and an increase in the unit weight of the upper soil. T3 and T7 are located in the fluctuation zone, while T2 and T6 are above the highest water level, so the former were wetted earlier. When settlement became differential, cracks developed, reducing the weight of the overlying soil and causing obvious decreases in the readings. Cracks 1–3 and cracks 4–6 are located above T1, T5 and T2, T6, respectively; therefore, the T2 and T6 curves show a declining segment within the rising trend, while T1 and T5, at the rear where the soil was not wetted, decreased only due to cracks 1–3 (Fig. 6b). The earth pressure at T2 and T6 decreased earlier but less than at T1 and T5, indicating that cracks 4–6 appeared earlier but were smaller than cracks 1–3, consistent with the macroscopic deformation images.

In Stage 2, points T2–T4 and T6–T8 were still strongly affected by water level fluctuations; since crack deformation in this stage was small and slow, it could not be reflected in the earth pressure data, which only show a positive correlation with the water level. The T1 and T5 curves kept decreasing because cracks 1–3 continued to expand; moreover, the declining rate increased significantly during drawdown, indicating that crack propagation accelerated during drawdown, which is unfavorable for slope stability (Fig. 6c).

(2) Pore water pressure

The pore water pressure data for the whole process are shown in Fig. 6d. Points at the same elevation show synchronization and a positive correlation with the water level: as the reservoir water rises, water infiltrates the slope and the water column above the sensor rises, increasing the reading; as the water level falls, groundwater seeps outward and the reading decreases. The pore water pressures in section 1 are generally higher than those in section 2, because the middle of the landslide is the core zone of soil compression, with longer seepage paths and a relatively closed structure; water migrating to the middle forms a locally closed environment, making pore water difficult to drain and pressure continuously accumulating to a peak, while the side areas near the model box boundary more easily establish hydraulic connection with the outside, promoting drainage and suppressing pressure rise.

In Stage 1, points K3 and K6 at the dead water level responded more rapidly to water level changes than K2 and K5 in the middle-upper fluctuation zone (Fig. 6e). The peak of each curve lagged behind the water level peak, because water migrates slowly in the soil and pore pressure transmission must overcome capillary forces and air

resistance; when the drawdown rate exceeded the drainage capacity of the soil, water could not be discharged in time, forming excess pore water pressure and a hysteresis accumulation phenomenon.

In Stage 2, the peak values of all points decreased significantly and appeared earlier than in the previous cycle, indicating weakened hysteresis (Fig. 6f). Repeated drying-wetting cycles, especially during drawdown, caused the cement between soil particles to dissolve and fine particles to be lost, leading to plastic deformation and particle rearrangement of the sliding-zone soil and forming a more stable pore structure and preferential seepage channels with stronger connectivity. This cumulative damage reduced the sensitivity of the soil to hydraulic changes, enhanced the synchronization between pore pressure response and water level change, increased drainage efficiency, and weakened the accumulation lag and peak value of pore water pressure.

(3) Water content

The water content data for the whole process are shown in Fig. 7a. Point H1, above the highest water level, was slightly affected: during the first rise, the soil was wetted by capillary action and the water content rose slightly, with a maximum of 10.37%. Point H2, in the fluctuation zone, shows an obvious positive correlation with the water level, with a maximum of 45.36%. Point H3, at the dead water level, rose rapidly and reached saturation when the water first rose to the dead water level, remaining stable afterwards, with a maximum of 45.76%.

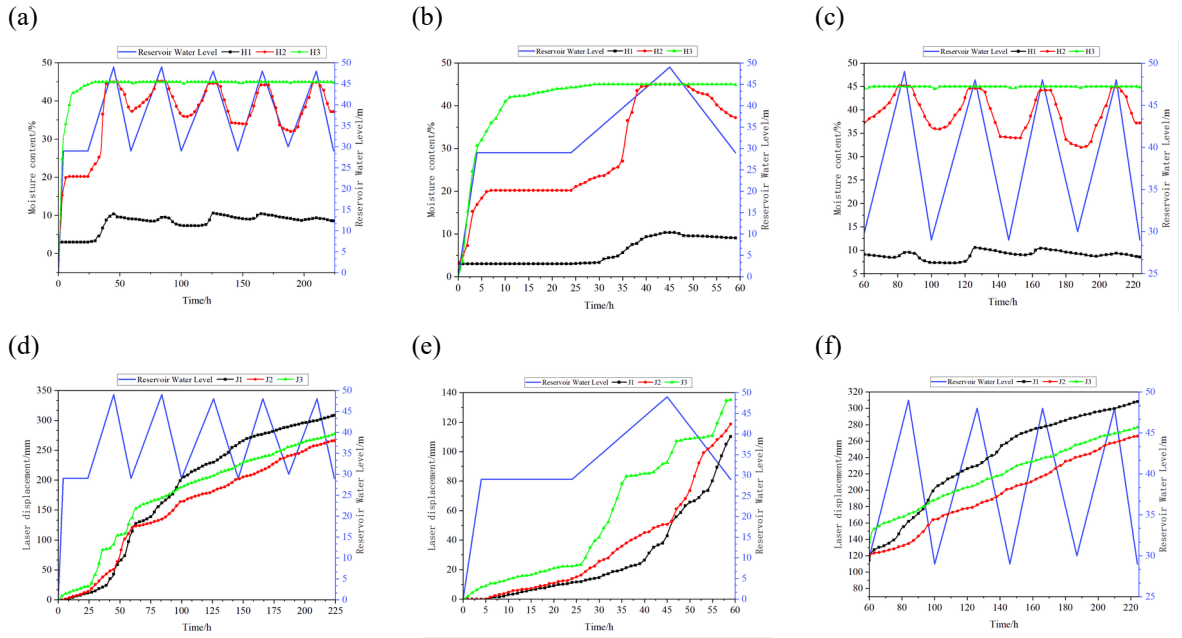


Fig. 7 Hydrological and displacement response of the physical model. (a–c) Water-content curves for the whole test, Stage 1 and Stage 2; (d–f) laser-displacement curves for the whole test, Stage 1 and Stage 2.

In Stage 1, the closer to the lower part of the slope, the faster the water content response (Fig. 7b). Due to capillary action, the water content began to rise before the water level reached the sensor elevation, and the growth rate accelerated significantly as the water level approached.

In Stage 2, under repeated cycles, the response of H2 became significantly faster, with steeper rising and falling slopes than in the previous cycle, and the minimum water content decreased with increasing cycle number (Fig. 7c). This behaviour is consistent with that of the pore water pressure: after preferential seepage channels formed, soil permeability increased and water migration paths shortened, making water easier to drain or infiltrate at the same water level, reducing the water-holding capacity and making the water content response more sensitive.

(4) Laser displacement

The laser displacement data for the whole process are shown in Fig. 7d. Three laser displacement points (J1, J2, J3) were arranged from top to bottom on the slope above the highest water level. The three curves are synchronized

and show an overall upward deformation trend with gradually decreasing slopes, indicating that the model deformed as a whole at a decreasing rate. The maximum cumulative displacements of J1, J2 and J3 are 308.3 mm, 266.1 mm and 277.1 mm, respectively. The rear edge above the highest water level deformed most, showing multi-level steps; the middle part was second, showing local collapses; and the part just above the highest water level deformed least, with multiple cracks. Deformation statistics for each stage are listed in Table 3.

In Stage 1, during the initial impoundment to the dead water level, J3 deformed first. As the water level rose further, the deformation rates of J1, J2 and J3 increased significantly, because the pore water pressure in the submerged area increased sharply, reducing effective stress and weakening the shear strength of the front-edge soil. J3 deformed first, followed by J2 and then J1, with maximum cumulative deformations of 135.2 mm, 118.7 mm and 110.3 mm, respectively. Deformation initiated at the front edge and then propagated to the middle and finally to the rear, decreasing from front to back, which is characteristic of progressive retrogressive deformation (Fig. 7e).

In Stage 2, the three curves show an overall upward trend with significantly lower slopes than in Stage 1 (Fig. 7f). After the first storage cycle of this stage, the cumulative deformation at the rear exceeded that at the front. During drawdown, the deformation rate increased to some extent, indicating that deformation propagated from the front to the rear at a lower rate, and that drawdown aggravates deformation and is unfavourable to slope stability, because the rapid dissipation of hydrostatic pressure removes support from the slope, while reverse seepage forces drive pore water outflow and induce excess pore water pressure accumulation, increasing the sliding force.

Table 2 Deformation statistics of the monitoring points at each stage

Stage	Point	Duration (h)	Cumulative deformation (mm)	Rate (mm/h)/h
Whole process	J1	224	308.3	1.38
	J2		266.1	1.19
	J3		277.1	1.24
Stage 1	J1	59	110.3	1.87
	J2		118.7	2.01
	J3		135.2	2.29
Stage 2	J1	165	198.0	1.20
	J2		147.4	0.89
	J3		141.9	0.86

The physical model simplifies the field slope structure and reservoir history because of constraints imposed by the model box, material preparation and boundary conditions; model sensors therefore do not correspond one-to-one with field monitoring points. The comparison is based primarily on deformation stages and their relationship to water level change. Field monitoring shows pronounced deformation after initial impoundment, followed by a gradual decline in average deformation rate, with further stepwise acceleration during subsequent drawdown. The model similarly shows strong deformation during initial wetting and the first storage cycle, lower average displacement rates in later cycles, and renewed acceleration during drawdown. Displacement also develops from the lower point J3 toward J2 and J1, consistent with the field tendency for deformation to extend from the front toward the middle and rear. Agreement in these stage-dependent responses and in the sequence of deformation propagation supports the model's ability to reproduce the main deformation characteristics of the Linbang landslide and provides a basis for interpreting its traction-driven retrogressive evolution.

Seepage erosion characteristics

The monitoring data indicate that seepage erosion at the slope front caused by water level fluctuations damages the soil structure and threatens landslide stability; this process was further examined using an underwater high-definition camera.

At the beginning of impoundment, reservoir water gradually infiltrated into the slope along the saturation line (Fig. 8a–e). Infiltration at the surface was significantly greater than inside the slope, so the hydraulic gradient of the surface soil was greater than that of the lower soil; according to Darcy’s law, water flows from the high-head area (slope surface) to the low-head area (slope interior), forming an inward hydraulic gradient. As the soil became saturated, the saturation line was eventually slightly higher than the water surface.

During water level drawdown, the pore water pressure inside the fluctuation-zone soil lagged behind the external water level change, forming an outward hydraulic gradient. Soil particles in the fluctuation zone migrated into the reservoir water during drawdown, creating more pores, while the soil below the dead water level had fewer pores. Comparing the surface of the fluctuation-zone and non-fluctuation-zone soils from the side of the model, the latter is covered by fine soil while the former is dominated by gravel, with a clear boundary between them. During the water level rise, the inward hydraulic gradient prevents particles from migrating outward, so the reservoir water remains clear; during drawdown, the outward gradient allows seepage to carry particles from the slope into the

reservoir water, making the water turbid, and the particles eventually settle at the slope front as the water recedes. After the first storage cycle, the bottom of the model box was still exposed with a maximum particle accumulation of 2 mm; after multiple cycles, the bottom was completely covered with an accumulation thickness of 7 mm.

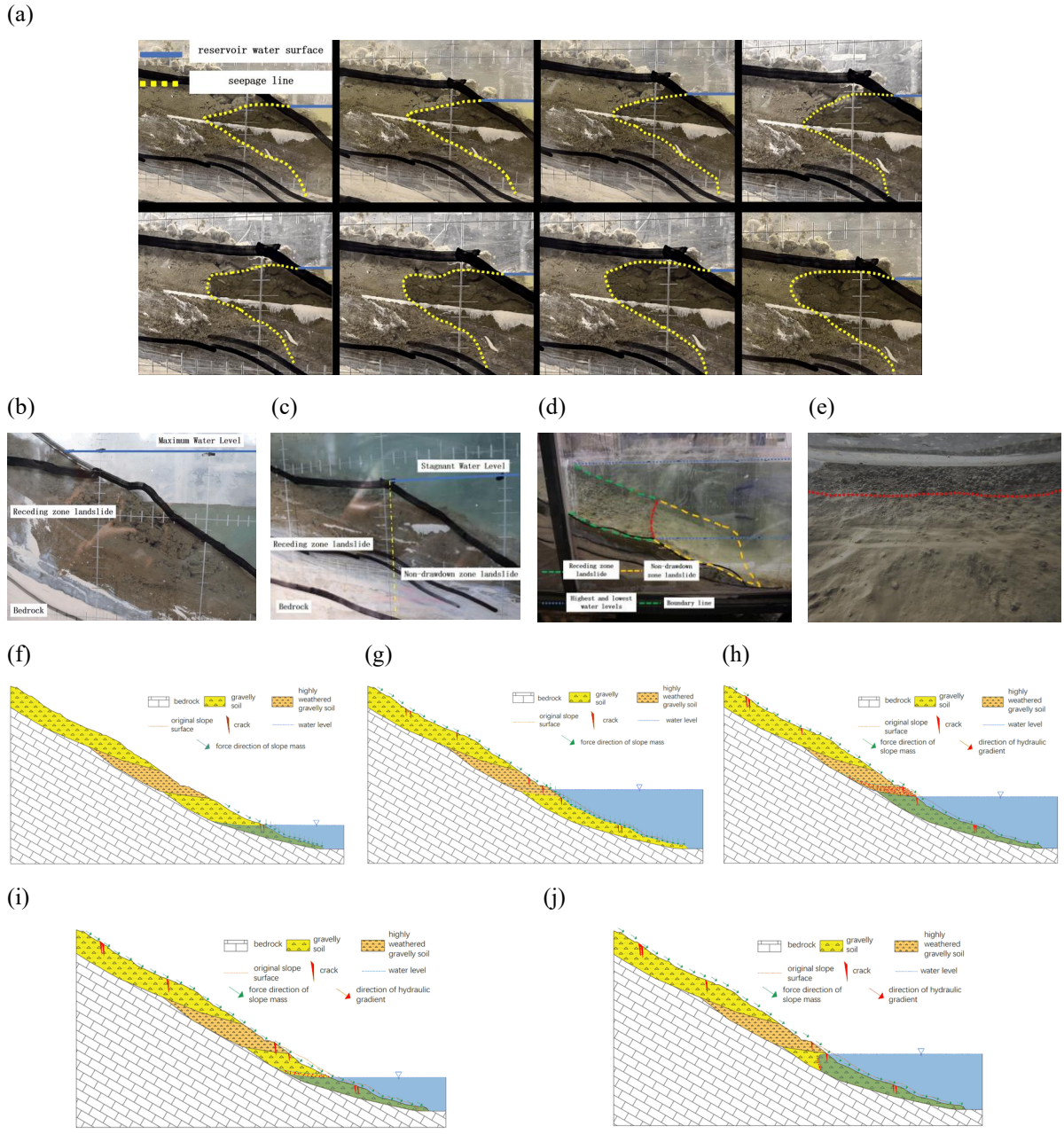


Fig. 8 Seepage erosion and staged deformation evolution. (a–e) Reservoir rise, soil infiltration, scour-zone development and comparison of the slip zone inside and outside the drawdown area; (f–j) deformation evolution during first rise to the dead water level, first rise to the high water level, early drawdown, drawdown to the middle level and the subsequent rise.

These observations indicate that during water level drawdown, seepage acts on the sliding mass, destroying the internal soil structure, weakening the shear strength, and aggravating landslide deformation and instability.

Deformation evolution mechanism of the multiple slip surfaces under reservoir water level fluctuations

The contact point between the normal storage level (1842 m) and the slope surface lies close to the outcrop of the strongly weathered phyllite gravelly soil layer (Fig. 4a), so that this layer, which forms sliding mass 2, is directly exposed to water level fluctuation. Sliding masses 1 and 3 consist of ordinary gravelly soil and differ from sliding

mass 2 in grain composition, permeability and shear response. The measured mean permeability coefficients of the three masses are 0.03168, 0.001226 and 0.03553 cm/s, respectively, and that of sliding mass 2 is about 1/26 and 1/29 of those of masses 1 and 3. From the natural to the saturated state, the cohesion of sliding mass 2 decreases from 16.3 to 14.3 kPa and its friction angle from 26.7° to 25.7°, whereas the cohesion of masses 1 and 3 decreases from 2.1 and 2.2 kPa to 0.1 and 0.2 kPa and their friction angles from 34.2 and 35.1 to 30.7 and 31.6 degrees. The action of reservoir water on the individual masses is therefore differentiated in both material and position: it alters the material state of the submerged gravelly soil and influences local deformation through different drainage adjustments, while movement of the lower mass 2 in turn modifies the support of the upper mass 3.

In terms of spatial position, the lower outcrop of the strongly weathered phyllite gravelly soil layer (weak zone) lies close to the normal storage level of 1842 m, and its lowest outcrop is below 1842 m, so that the outcrop essentially coincides vertically with the 1802–1842 m water level fluctuation zone. This position determines the way in which reservoir water acts on the layer. If the weak zone outcropped above the fluctuation zone, reservoir water could wet it only slightly through capillary action, as at H1 above the highest water level, where the water content remains at about 10.37%. If it outcropped below the dead water level, its material state would stabilize once saturated, as at H3 at the dead water level, where the water content no longer varies with water level cycles after saturation during initial impoundment (45.76%). Because the outcrop lies within the fluctuation zone between these two situations, the water content varies continuously with water level fluctuation, as at H2 in the fluctuation zone (up to 45.36%; Fig. 7a), and the pore water pressure peak always lags behind the water level peak, making this layer the part of the slope where the hydraulic state changes most strongly and most repeatedly. The action of reservoir water on the landslide is thus amplified within this layer and transmitted upwards. The slip-surface elevations identified from the borehole inclinometers also fall mainly within this zone, which is consistent with the position described above.

The influence of this position on the subsequent traction deformation is first reflected in the timing of deformation. Because the outcrop is directly exposed to water level fluctuation, its water content and pore water pressure respond earlier than the upper masses: in the model the lower measuring point J3 starts to move before J2 and J1 (Fig. 7d,e), and the earth pressure at T2 and T6 (beneath cracks 4–6) decreases earlier than at T1 and T5 (beneath cracks 1-3; Fig. 6b), so that deformation spreads progressively from the submerged part towards the upper slope. Second, the layer plays two roles at the same time: it provides direct support for the upper masses and is also the part that is immersed longest and softened most. After initial impoundment, its settlement and softening weaken the support of the upper masses, the space available for their movement increases, cracks open at the boundaries between masses, and relative movement between the masses is thereby drawn out by traction.

Third, the combined disadvantage of material and position provides the hydraulic basis for differential deformation. This layer has a higher fine-particle content and a stronger water retention capacity, and its measured mean permeability coefficient is only 0.001226 cm/s, about 1/26 and 1/29 of those of masses 1 and 3. During a single drawdown, therefore, the external water level falls rapidly while internal drainage within this layer is slow, and the head difference between the slope and the reservoir accumulates and is released mainly in this layer. The adjacent gravelly soils, whose permeability is an order of magnitude higher, can follow the reservoir level more quickly, and the difference in response rate is expressed directly as relative displacement between masses and continued opening of the boundary cracks. Finally, this action is cumulative: the material state continues to change over drawdown cycles, so that even when the average deformation rate of later cycles declines, a single drawdown can still trigger stepwise deformation (Fig. 8f–j), which is consistent with the coexistence of long-term deceleration and drawdown-stage steps identified in the multi-field analysis. In addition, because the outcrop lies within the fluctuation zone, the effective stress on the potential sliding surface is most strongly affected by the water level: in the numerical simulation the maximum effective stress at the monitoring points decreased to as low as 204 kPa during water level rise and recovered to 633 kPa during drawdown, and since the degradation of strength parameters is irreversible, the repeated rise and fall of the resisting capacity superimposed on this cumulative degradation further amplifies the risk of instability during drawdown. This spatial relationship also indicates that the outcrop of the layer and a certain range above and below it should be treated as a priority zone for monitoring and treatment.

During initial impoundment, the gravelly soil absorbs water, becomes wetted and gradually saturated, and its initial material state changes; combined with the natural and saturated material tests, the change in shear parameters and the adjustment of self-weight of the submerged gravelly soil explain the initial settlement and sliding. In the model, after sliding mass 2 deformed, a crack appeared at the boundary between masses 2 and 3 and multi-level steps formed in the upper part of mass 3; J3, J2 and J1 started to move in turn, reflecting the transfer of deformation from the front towards the rear. The deformation transfer process during initial impoundment is shown in Fig. 8f,g.

The key change during drawdown is that the decrease in external water level and the internal drainage are out of phase. The pore pressure peak lags behind the water level peak, and the displacement rate increases during drawdown, indicating that the time required for internal hydraulic adjustment controls the deformation response. When the external water pressure support has already decreased, a relatively high head is still maintained inside the slope,

forming an outward hydraulic gradient; residual pore pressure affects the effective stress, and the outward seepage promotes continued deformation of the submerged part. The expansion of boundary cracks and the deepening of the upper steps during this stage link the local movement under hydraulic action with the traction of the upper masses, and explain why different masses show different deformation times and magnitudes within the same drawdown. The evolution at the beginning of drawdown and when the water level has fallen to the middle level is shown in Fig. 8h,i.

Repeated drawdown also affects the structure of the gravelly soil through particle migration. The images show loss of fine particles in the fluctuation zone, exposure of coarse particles at the surface and turbid reservoir water, and the accumulation at the front increased from 2 mm after the first cycle to about 7 mm at the end of the test, indicating a change in local grain composition and pore conditions. These phenomena are consistent with the subsequent decrease in pore pressure peaks, the weakened lag and the faster water content response of H2, which supports the interpretation that adjustment of the drainage paths participates in the cyclic response.

The subsequent rise differs from initial impoundment: part of the soil has been saturated for a long time and the initial state of the previously wetted zone has already changed, while the inward seepage inhibits downslope movement. The subsequent rise therefore produces a smaller incremental deformation, in contrast to the accelerating response during first wetting. At the same time, the pore pressure lag weakens while the boundary cracks, collapses and rear steps continue to accumulate, indicating that adjustment of the drainage conditions affects the response to a single water level cycle, whereas the existing cracks and the changed support between masses allow the traction process to continue. The deformation evolution during the subsequent rise is shown in Fig. 8j.

From the perspective of the evolution of the multiple slip surfaces, reservoir water acts first on the submerged gravelly soil and drives local deformation through immersion-induced material change, drainage lag and particle migration; the differences in response produced by different materials and positions of exposure are expressed collectively as relative movement between masses and boundary cracks; and the change in lower support then draws the upper masses forward, so that movement extends towards the rear along the masses controlled by the different slip surfaces. The link between the action of reservoir water and the slope structure thus forms a transfer process of deformation of the submerged part, differential displacement at the boundaries and traction of the upper masses, which explains the staged characteristics of the Linbang landslide: acceleration during initial impoundment, stepwise movement during drawdown and deceleration during the subsequent rise.

Multi-field coupled numerical simulation

On the basis of the physical model test, numerical simulation was further conducted under different reservoir water level variation rates coupled with rainfall conditions, to analyze the evolution laws of the seepage, stress and displacement fields, explore the potential connections among them, and clarify the influence of multi-field evolution on the landslide mechanism and the controlling effect of water level fluctuations on landslide stability.

Model setup and parameter selection

Based on the main section of the Linbang landslide, a calculation model was established in the SEEP/W module of Geo-Studio (Fig. 9a). Based on engineering analogy and experience, the right boundary was set as a constant head boundary (maximum 1842 m, minimum 1802 m). The seepage model was imported into SLOPE/W to build a stability calculation model and into SIGMA/W to build a deformation calculation model. Monitoring points H01–H05 were arranged inside the slope at elevations of 1802 m, 1812 m, 1822 m, 1832 m and 1842 m. Finite-element stability analysis and transient saturated-unsaturated seepage modelling provide the basis for evaluating the response to rapid water-level change (Biniyaz et al. 2022; Griffiths and Lane 1999; Yu et al. 2020).

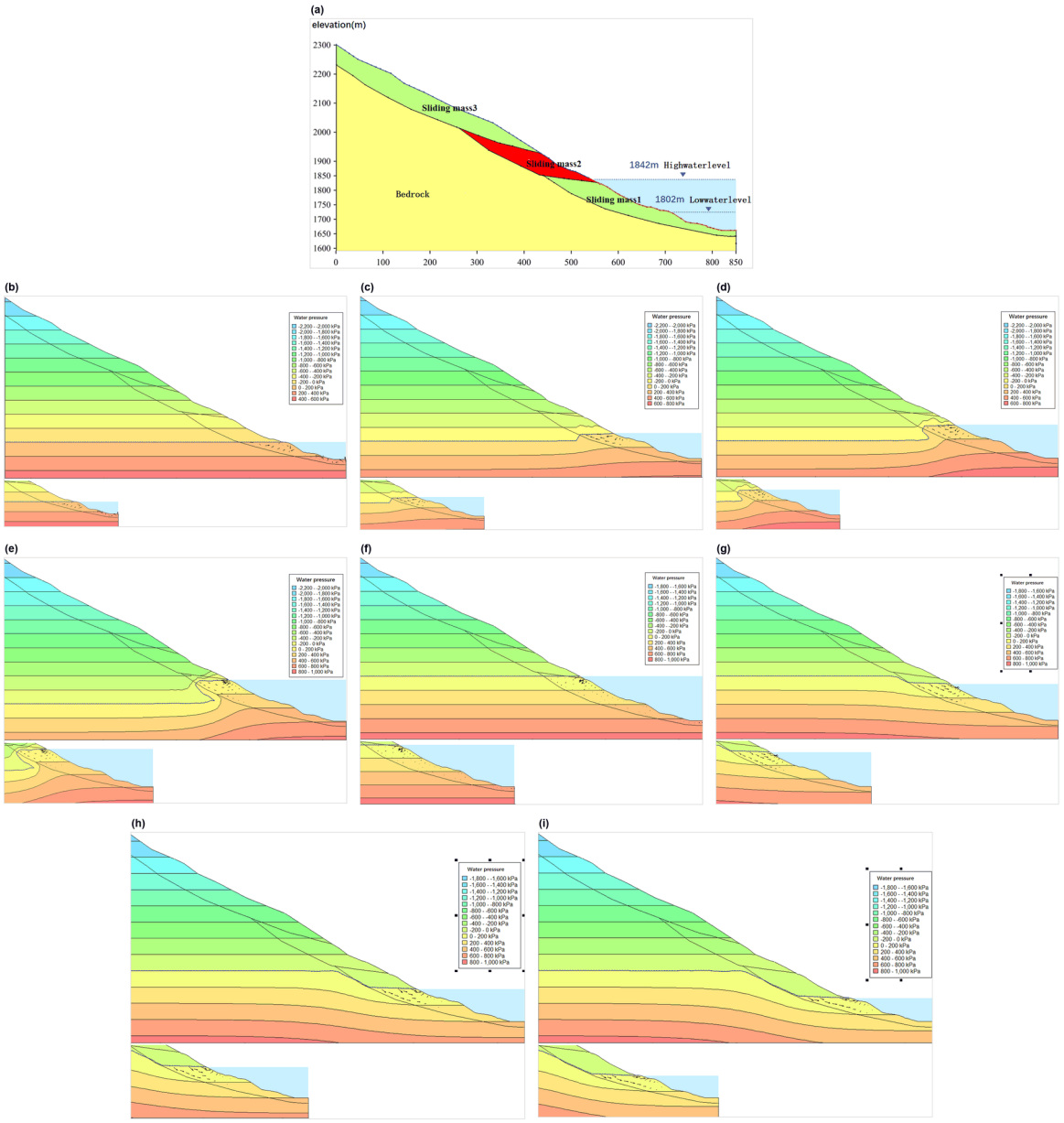


Fig. 9 Representative seepage fields for the fastest water-level change (v = 1.3 m/d). (a) Generalized seepage model; (b–e) four representative stages during water-level rise; (f–i) four representative stages during water-level decline.

Combining the laboratory soil parameters with the survey data, the geotechnical materials were divided into gravelly soil of the sliding mass and phyllite-dominated gravelly soil. Considering three conditions (natural, rainstorm and underwater), the parameters of each soil layer are listed in Table 3. The permeability coefficient of the gravelly soil is k = 0.0315 cm/s, and that of the strongly weathered gravelly soil is k = 0.0012 cm/s.

Table 3 Strength parameters of each soil layer

Soil type	Natural			Rainstorm			Underwater	
	γ (kN/m³)	C (kPa)	φ (°)	γ (kN/m³)	C (kPa)	φ (°)	C (kPa)	φ (°)
Gravelly soil	19.5	2.1	34.2	20.1	0.1	33	0	31
Phyllite-dominated gravelly soil	21.3	16.3	26.7	22.7	14.3	25.7	10	23
Blocky soil	20.0	0	36	20.5	0	35	0	32

Saturated-unsaturated seepage field characteristics

Water level rise from the dead water level to the normal storage level

According to the measured reservoir water level data, the maximum variation rate in the Linbang reservoir area is 1.3 m/d and the minimum is 0.43 m/d. Two uniform rise conditions were set—1.3 m/d (completed in 30 d) and 0.43 m/d (completed in 90 d)—to simulate the seepage field evolution during the water level rise from the dead water level (1802 m) to the normal storage level (1842 m), focusing on the dynamic response of the saturation line and pore water pressure distribution (Fig. 9b–e and Fig. S1).

The results show that seepage is concentrated at the slope toe, where seepage is most active and the soil is easily disturbed. As the water level rises, the saturated area increases, the external water level gradually exceeds the internal groundwater level, and reservoir water recharges the groundwater, so the seepage direction points from outside into the slope, and the saturation line concaves upward from the contact zone; the faster the rise, the greater the concavity. The rise rate is positively correlated with the curvature radius of the saturation line: the faster the rise, the wider the spacing of adjacent equipotential lines and the steeper the hydraulic transition zone. After the water level stabilizes, the evolution rate of the saturation line decays, because the hydraulic gradient gradually weakens as the saturation line adjusts, weakening the seepage driving force and lengthening the seepage path.

The dynamic response of the seepage field shows a significant dependence on medium properties: during water level rise, the migration of the saturation line exhibits a phase lag, spatially manifesting as a linear hydraulic transition zone inclined toward the slope interior. The slope is simultaneously subjected to hydrostatic buoyancy and seepage pressure, and the seepage force is positively correlated with the hydraulic gradient. The permeability coefficient k controls the seepage field morphology (Table S2, Fig. S2): the larger k is, the faster reservoir water enters the slope, the larger the saturated area, and the weaker the hysteresis; the smaller k is, the more significant the hysteresis.

Pore water pressure data (Fig. S3, Tables S3 and S4) show that the pore water pressure of all points rises with the water level. Point H1 (near the dead water level of 1802 m) increases linearly, whereas the other points exhibit abrupt inflection points, confirming the hysteresis effect. The increase in pore water pressure at the same point grows as the elevation decreases. In summary, during water level rise, the seepage field is jointly affected by the permeability coefficient and the rise rate: the smaller the permeability coefficient and the faster the rise, the more obvious the hysteresis; with high permeability, reservoir water quickly enters the slope, the saturated area expands, and pore water pressure increases rapidly.

Water level decline from the normal storage level to the dead water level

The seepage process during the uniform decline from the normal storage level (1841 m) to the dead water level (1802 m) was simulated at two rates, 1.3 m/d (30 d) and 0.43 m/d (90 d), to analyze the variations in the saturation line and pore water pressure (Fig. 9f–i and Fig. S4).

As the decline rate decreases, the variation of the front-edge saturation line weakens; the faster the decline, the stronger the hysteresis of the internal groundwater level, especially at the interface between the bedrock and the gravelly soil layer, where a sudden change of the front-edge saturation line occurs. This phenomenon gradually disappears after the water level stops falling. Under rapid drawdown, the hydraulic gradient inside and outside the slope is steeper, and the dissipation of pore water pressure significantly lags behind the water level decline.

Comparison of the seepage field under different permeability coefficients (Fig. S5) shows that when the seepage rate of the slope is much greater than the rate of reservoir water change, the internal groundwater level adjusts in time, the hysteresis is insignificant, and the saturation line is basically horizontal; when the seepage rate is lower than the decline rate, the groundwater level is higher than the reservoir level and declines with an obvious lag, the saturation line near the slope surface drops more sharply, and the front-edge curve concaves downward, forming an outward seepage force.

Pore water pressure data (Fig. S6, Tables S5 and S6) show that the pore water pressure of all points decreases with the water level. Point H5 (near the highest level of 1842 m) changes linearly, whereas the other points exhibit inflection points at which the rate of decrease slows. The initial and final pore water pressures are basically the same under the two decline rates, but under rapid drawdown the dissipation is faster and the inflection points appear earlier. In summary, during water level decline, the smaller the permeability coefficient and the faster the decline, the more obvious the hysteresis and the more prominent the outward seepage force.

Rainstorm infiltration at the dead water level

During rainfall, rainwater gradually infiltrates the shallow slope deposits, raising the water content of the surface soil. As infiltration continues, water migrates vertically and preferentially reaches the aquiclude at the slope toe, where the seepage path is short, forming a local perched-water zone; the saturation of this zone increases progressively, eventually forming an infiltration interface with hydraulic boundary characteristics. The infiltration capacity peaks at the initial stage and then decreases: initially, the steep hydraulic gradient of the surface soil drives rapid infiltration; as the wetting front advances deeper, the matrix suction gradient flattens, the infiltration rate decays, and a stable seepage stage is finally reached.

Based on meteorological data of the Dadu River basin, the typical rainstorm intensity in the Linbang area reaches 40 mm/d. A numerical model was built to simulate the effect of 3 consecutive days of 40 mm/d rainfall on the seepage field with the water level held at the dead water level (1802 m). The results (Fig. S7) show that the thin landslide body and short seepage path allow rainwater to quickly reach the weakly permeable layer, forming a preferential seepage channel along the bedrock surface and finally a confluence zone near the reservoir water level; under continuous rainfall, the saturation line rises systematically, the transient saturated zone expands, and matrix suction weakens continuously. The rear of the slope is weakly affected, while the area near the reservoir water level responds significantly.

Rainstorm infiltration at the normal storage level

With the water level held at the normal storage level (1841 m), a 3-day rainstorm with q = 40 mm/d was simulated (Fig. S8). During continuous rainfall, most rainwater is discharged as surface runoff, so the wetting front develops shallowly and advances slowly; pore water pressure accumulates at the rock-soil interface, while the unit weight of the sliding mass increases, forming a mechanical environment unfavorable for stability. The deposit has strong permeability, but limited by the thin sliding mass and the underlying weakly permeable bedrock, most infiltrated water forms runoff channels along the rock-soil interface.

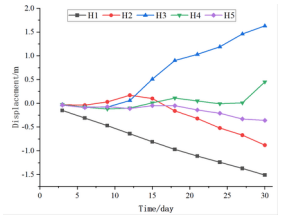
Monitoring data show that as rainfall continues, the saturation line rises significantly, the saturated zone expands continuously, and the pore water pressure at the rock-soil interface increases over time. The evolution of the seepage vector field shows that at the initial stage the flow directions are disordered, with some paths infiltrating at 45° oblique to the interface and others migrating parallel to it toward the front edge; after the infiltration front reaches the interface, the seepage direction adjusts to parallel movement along the interface, aggravating the expansion of the front-edge saturated zone.

Displacement and stress field characteristics

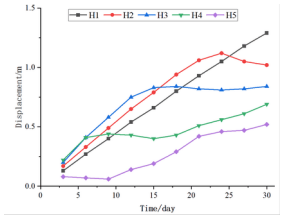
(1) Displacement field

Stress-seepage coupling analysis was conducted using the SIGMA/W module, with the displacement reset to zero before impoundment. When the water level rose from 1802 m to 1842 m, the monitoring results show that point H1 at the dead water level, which had been saturated underwater for a long time, was basically unaffected in material properties by the water level rise, and only moved in the negative x direction under the inward seepage force, with a maximum displacement of 1.51 m (Table S7); points H2–H4 were gradually submerged as the water level rose, and when the water reached their elevations, the soil softened and its mechanical properties deteriorated, so the displacement showed a downslope (positive x) trend (Fig. 10a), which then slowed or even reversed under the inward seepage force. This indicates that the displacement response of points in the water level fluctuation zone is controlled by the balance between the soil softening effect and the seepage force effect.

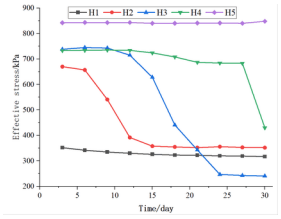
(a)


H1 H2 H3 H4 H5
Displacement/m
Time/day

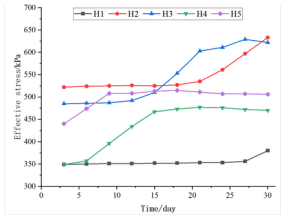
(b)


H1 H2 H3 H4 H5
Displacement/m
Time/day

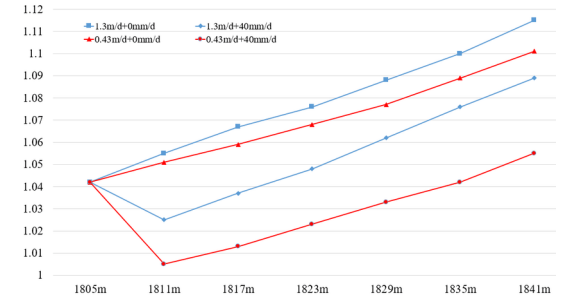
(c)


H1 H2 H3 H4 H5
Effective stress/kPa
Time/day

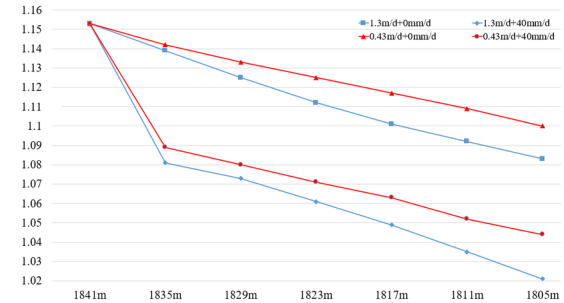
(d)


H1 H2 H3 H4 H5
Effective stress/kPa
Time/day

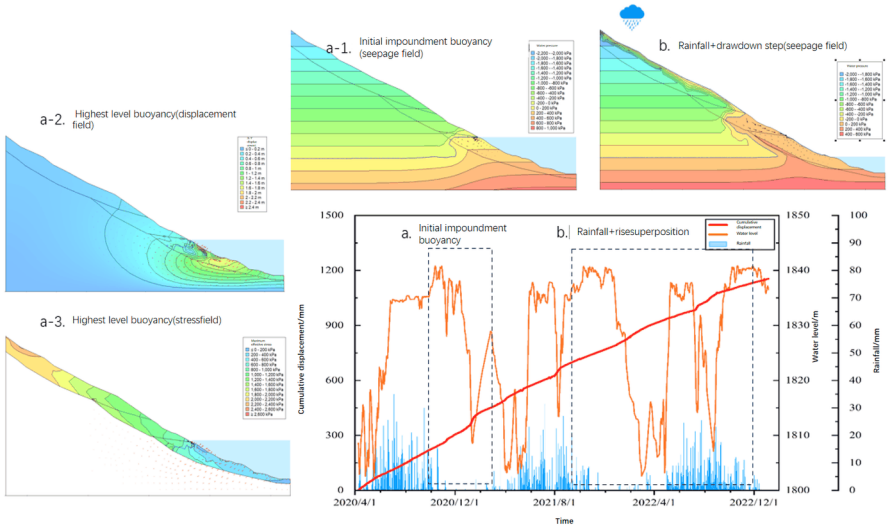
(e)


1.3m/d+0mm/d
1.3m/d+40mm/d
0.43m/d+0mm/d
0.43m/d+40mm/d
1805m
1811m
1817m
1823m
1829m
1835m
1841m

(f)


1.3m/d+0mm/d
1.3m/d+40mm/d
0.43m/d+0mm/d
0.43m/d+40mm/d
1841m
1835m
1829m
1823m
1817m
1811m
1805m

(g)


a-1. Initial impoundment buoyancy (seepage field)
b. Rainfall+drawdown step(seepage field)
a-2. Highest level buoyancy(displacement field)
a-3. Highest level buoyancy(stressfield)
a. Initial impoundment buoyancy
b. Rainfall+risesuperposition
Cumulative displacement/mm
Water level/m
Rainfall/mm
Time
2020/4/1
2020/12/1
2021/8/1
2022/4/1
2022/12/1

(h)

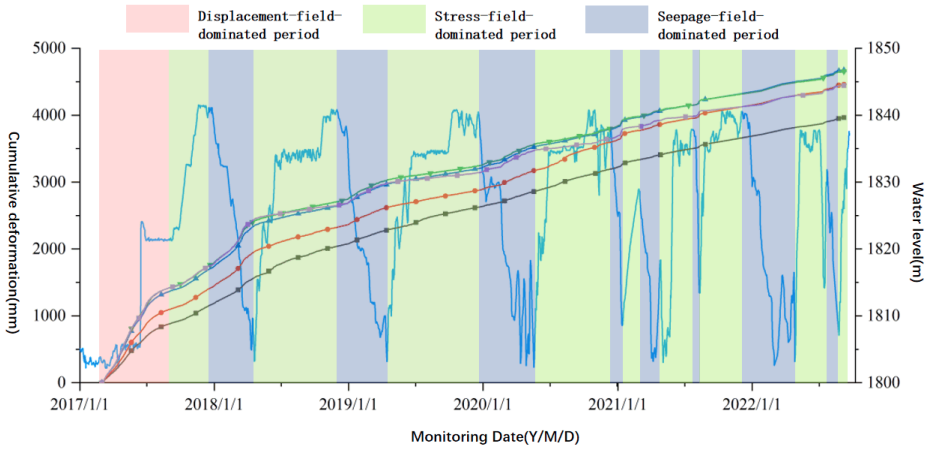

Displacement-field-dominated period
Stress-field-dominated period
Seepage-field-dominated period
Cumulative deformation(mm)
Water level(m)
Monitoring Date(Y/M/D)
2017/1/1
2018/1/1
2019/1/1
2020/1/1
2021/1/1
2022/1/1

Fig. 10 Coupled multi-field response and stability analysis. (a,b) x-displacement during water-level rise and decline; (c,d) maximum effective stress during rise and decline; (e,f) stability coefficient under coupled water-level rise or decline and rainfall; (g) correlations among multi-field responses and deformation; (h) dominant evolution periods.

During water level decline, the maximum horizontal displacement concentrated in the middle-lower part of the slope, while the maximum vertical displacement was at the slope top (Table S8); as the water level continued to fall, the horizontal displacement extremum decreased while the vertical extremum increased (Fig. 10b). The mechanism is as follows: in the early decline stage, the unloading of hydrostatic pressure on the slope surface and the outward dynamic water pressure jointly dominated the horizontal displacement; in the later stage, as the saturation line fell, pore water pressure dissipated and the dynamic water pressure decayed, the consolidation effect of the soil became prominent, and vertical settlement became the dominant displacement component. The displacement mode thus transformed dynamically from horizontal-dominated to vertical-dominated.

(2) Stress field

The maximum effective stress at equilibrium before impoundment was calculated, and the water level was then raised from 1802 m to 1842 m. The maximum effective stress of all points decreased with the rising water level, down to a minimum of 204 kPa; the effective stress at the slope toe was low, in the range of 300–400 kPa without obvious stress concentration, while near the fragmented sliding mass it was larger, in the range of 800–900 kPa (Table S9, Fig. 10c).

Under water level rise, the effective unit weight of the soil changes from natural to buoyant, producing a dual mechanical effect: on one hand, the reduction of the downslope gravity component (sliding force) reduces the driving force of instability, improving stability; on the other hand, the reduction of the normal gravity component (normal pressure) weakens the shear strength parameters of the potential sliding surface, degrading stability. This coupling of positive and negative effects determines the dynamic evolution of slope stability during water level rise.

When the water level fell from 1842 m to 1802 m, the maximum effective stress of all points increased overall, up to a maximum of 633 kPa, while the effective stress at the slope toe remained low, in the range of 350–400 kPa without obvious stress concentration (Table S10, Fig. 10d).

Water level decline increases the effective unit weight of the soil, equivalent to applying an additional load to the slope. The buoyancy response evolves oppositely to that during the rise: as buoyancy decays, both the anti-sliding force and the sliding force increase, but the latter increases more significantly. In the early decline stage, the saturation line mainly acts on the upper sliding zone, where the buoyancy reduction is significant, so the increment of the sliding force dominates, forming the main factor of stability degradation.

Stability analysis under coupled water level variation and rainfall conditions

Combined with the flood-season water level changes and regional rainfall of the Linbang landslide, transient stability analysis was conducted with two water level variation rates (0.43 m/d and 1.3 m/d) coupled with no-rainfall and 40 mm/d rainstorm conditions. The simulation scheme is listed in Table S11.

Stability under coupled water level rise and rainfall

The water level rise from 1802 m to 1841 m was treated as a dynamic process, with every 6 m of rise as one time step (6 steps in total). Boundary conditions were set with no rainfall, 3-day rainfall intensities of q = 50, 100 and 200 mm/d, and rise rates of v = 1, 2 and 3 m/d, and the stability coefficients at 1808, 1814, 1820, 1826, 1832 and 1838 m were obtained (Fig. 10e).

Fig. 10e shows the variation of the stability coefficient under combined rainfall intensity and rise rate conditions: with the same permeability coefficient and rise rate, the greater the rainfall intensity, the more significant the decrease of the stability coefficient; with fixed permeability and rainfall intensity, the greater the rise rate, the smaller the attenuation. Overall, water level rise reduces slope stability, but the greater the rise rate, the gentler the declining trend.

This behaviour is attributed to the fact that, in the early rise stage, the unsaturated zone shrinks and matrix suction decays, directly weakening the shear strength; meanwhile, the highly permeable deposit concentrates reservoir

water action on the anti-sliding section, and the buoyancy weight-loss effect significantly reduces the front-edge anti-sliding force. Because the slope material has a relatively high permeability, differences in the timing of groundwater adjustment among the rise-rate scenarios are small. Thus, although the water level rise rate affects the reduction in the stability coefficient, its influence on the magnitude of that reduction is relatively limited.

Stability under coupled drawdown and rainfall

The water level decline from 1841 m to 1802 m was treated as a dynamic process, with every 6 m of decline as one time step (6 steps in total). Boundary conditions were set with no rainfall, 3-day rainfall of q = 40 mm/d, and decline rates of v = 0.43 and 1.3 m/d, and the stability coefficients at 1835, 1829, 1823, 1817, 1811 and 1805 m were obtained (Fig. 10f).

Fig. 10f shows that with constant permeability and decline rate, the greater the rainfall intensity, the greater the attenuation of the stability coefficient; with fixed permeability and rainfall intensity, the greater the decline rate, the more significant the attenuation. During continuous decline, the slope stability decreases progressively, while the rainstorm infiltration stage triggers stepwise instability.

This behaviour is attributed to the fact that the faster the decline, the steeper the hydraulic gradient inside and outside the slope and the stronger the dynamic water pressure, while the dissipation of matrix suction in the unsaturated zone accelerates; superimposed with the softening and strength parameter attenuation caused by long-term reservoir water immersion, the effective stress of the anti-sliding section decreases while the driving force of the sliding section increases, finally manifesting as rapid stability attenuation. It can be seen that the water level variation rate dominates the instability process by regulating the spatiotemporal distribution of seepage forces, and the coupling of seepage forces and soil strength degradation during decline nonlinearly amplifies the instability risk.

Overall, faster reservoir drawdown steepens the hydraulic gradient between the slope and the reservoir, strengthening the seepage force and accelerating the loss of matric suction in the unsaturated zone. These effects reduce effective stress in the resisting part of the slope and increase the downslope driving force, resulting in a more rapid decline in stability. This response illustrates how the rate of water level change affects slope stability through the spatial and temporal distribution of seepage forces.

Multi-field evolution of the Linbang landslide

Reservoir-bank landslides show significant hydrodynamic sensitivity, and their instability events mostly occur during dynamic reservoir regulation, especially during rapid drawdown. Triggered by external dynamic factors such as water level fluctuations and rainfall, the hydrogeological environment of the bank slope changes, easily inducing overall or local instability. Deformation caused by water level variation mainly occurs during rapid drawdown, and the deformation and stability of the landslide are closely related to the variation rate and the permeability of the landslide body.

(1) Seepage field: the pore water pressure in and below the water level fluctuation zone is highly sensitive to water level changes, and the response becomes less timely with increasing distance from the slope surface. The surface layer responds most rapidly, while internal points show a time-lag effect. During rapid drawdown, the front-edge pore water pressure drops rapidly and sharply, while during the rise it increases sharply. This differentiated hydraulic response makes the drawdown process more detrimental to stability. Rainfall significantly disturbs the stability of the shallow sliding surface, and its influence pattern is dynamically related to the reservoir water state: water level changes regulate the water-air migration channels during rainfall infiltration, altering the action range and transmission path of the two-phase fluid. When the water pressure of the saturated zone at the slope top is transmitted to the front edge through the air pressure of the unsaturated zone, water level decline locally lowers the groundwater level of the anti-sliding zone, moves the water-air overflow zone downward and forms an outward air pressure gradient, thereby enhancing the water-air coupling force in the anti-sliding zone and aggravating the instability risk.

(2) Displacement field: under actual conditions, different parts of the landslide show differentiated deformation modes. The maximum displacement concentrates in the water level fluctuation zone, with pronounced movement toward the free face, while the middle-rear part deforms less. The horizontal displacement in the fluctuation zone is inversely related to water level change: it increases significantly during the rise and decreases during the decline. The middle part is jointly controlled by water level fluctuations and rainfall, with small horizontal displacement during the rise and intensified changes during the decline. The rear part is mainly affected by continuous rainfall, showing slowly increasing small deformation.

(3) Stress field: during water level rise, the increased pore water pressure in the front-edge saturated zone significantly reduces the effective stress and the shear strength, and the shear stress gradually transfers toward the rear. During decline, the adjustment is reversed: pore pressure dissipation restores the effective stress, and the front-

edge shear stress is significantly strengthened compared with the rise stage. This stress redistribution is directly related to the dynamic change of hydraulic boundary conditions.

(4) Multi-field evolution laws: based on the above analysis and the measured data, the correlations among the multi-field responses, rainfall, reservoir water level and landslide deformation are summarized (Fig. 10g); the joint action mechanism of multiple fields in different periods is further generalized, and the deformation process is divided into three dominated periods according to the influence of each field (Fig. 10h): the displacement-field-dominated period (from initial impoundment to the dead water level), the stress-field-dominated period (water level rise), and the seepage-field-dominated period (water level decline).

Displacement-field-dominated period: during initial impoundment, the water level rises from the natural state to the dead water level, and the slope gradually becomes saturated. The rock and soil are softened for the first time, the strength decreases significantly, and the increased self-weight after saturation induces settlement deformation, with point H1 deforming up to 1.51 m. At this time, the seepage field has not yet formed a stable saturation line, the adjustment of the stress field is small, and the cumulative displacement is the most direct response.

Stress-field-dominated period: as the water level rises, the seepage field stabilizes, and the continuous adjustment of the stress field becomes the dominant factor. The increased pore water pressure reduces the effective stress, while the self-weight of the slope increases from the unsaturated to saturated state, increasing the sliding component and moving the shear stress toward the upper part of the sliding mass. However, the hydraulic gradient points into the slope, and the seepage force provided by the seepage field offsets part of the sliding component, so that the displacement finally decelerates.

Seepage-field-dominated period: during rapid decline, the pore water pressure inside the slope cannot be discharged in time, generating an outward seepage force. The seepage force is directly superimposed on the gravity stress field, causing a sudden increase in the sliding force; meanwhile, the effective stress recovers briefly but the shear strength fails to return to its original value, further aggravating deformation. The final deformation is manifested as the hysteretic stepwise change of the displacement field.

The displacement-, stress- and seepage-field-dominated periods correspond respectively to the acceleration, deceleration and stepwise deformation stages of landslide evolution.

Discussion

Mechanism of deformation driven by reservoir water level fluctuations

Building on the process observations presented above, this section generalizes the mechanical mechanism of deformation driven by reservoir water level fluctuations. Both field monitoring and the model test show strong deformation during initial impoundment, followed by a decline in the average deformation rate but renewed acceleration during drawdown. This sequence can be interpreted in terms of softening of the submerged soil, changes in seepage direction and adjustments in support between adjacent sliding masses. This sequence is consistent with the self-adaptive response reported for reservoir landslides under repeated water-level cycles (Li 2021) and with the control of groundwater-level changes on displacement response (Corominas et al. 2005). Seepage-driven deterioration can also promote progressive failure in seepage-sensitive rock materials (Chen et al. 2023). Pore water pressure, earth pressure and displacement records describe the hydraulic response, load redistribution and movement, respectively; their response sequence provides evidence for progressive failure.

During initial impoundment, reservoir water advances into the slope along the wetting front. Matric suction decreases in the unsaturated zone and pore water pressure increases in the saturated zone, affecting effective stress and shear resistance. Buoyancy reduces the effective weight of the submerged mass, while immersion-induced softening promotes settlement at the front and weakens support for the upper slope. These effects are superimposed in the same part of the slope, so that the submerged part loses its stable support and begins to move before the upper masses, which constitutes the starting condition for the traction deformation.

During subsequent water level rises, the hydraulic gradient points into the slope and the seepage force opposes potential sliding, while external hydrostatic pressure provides additional support. Cracks formed during the first deformation episode provide pathways for water movement. The lower pore pressure peaks and reduced lag in later cycles are consistent with an adjustment of drainage conditions. These effects help explain the decline in average deformation rate, although they do not imply that effective stress increases everywhere during a water level rise. Wetting-induced softening and hydraulic support coexist, and their combined effect depends on local material properties and loading conditions.

During drawdown, external water pressure decreases while drainage within the slope lags behind, creating an outward hydraulic gradient. Outward seepage increases the downslope driving force, and residual pore water pressure limits the recovery of effective normal stress and frictional resistance. The delayed drainage of the submerged

weak zone further amplifies this effect, which is expressed as stepwise deformation during drawdown (Fig. 7f). Drawdown deformation therefore reflects both the changing hydraulic boundary and the effects of preceding softening and structural deterioration.

These local processes develop into progressive retrogressive deformation through changes in support between the masses. Settlement and movement at the front reduce restraint on the middle mass; its movement toward the free face then draws the rear mass forward, producing the tension cracks and multi-level steps observed in the field and model (Fig. 1c and Fig. 5c–f). Crack extension also changes drainage pathways, progressively modifying the hydraulic response in later cycles. A decline in the long-term average deformation rate can therefore coexist with stepwise acceleration during individual drawdown stages. This adjustment does not mean that fine-particle loss or local structural deterioration has ceased.

Deformation zoning and the sensitivity of Zone I to drawdown

Field Zones I, II and III represent strong deformation at the front, traction in the middle and passive dragging at the rear, respectively. The physical model primarily captures interactions between individual sliding masses within Zone I: pore pressure and water content vary with the reservoir cycle, displacement begins at J3 before J2 and J1, and the boundaries between masses progressively open. Earlier earth pressure decreases at T2 and T6, followed by continued decreases at T1 and T5, indicate changes in support and load redistribution after deformation of the lower mass. Numerical results further show that seepage direction and the phreatic surface near the fluctuation zone change during impoundment and drawdown, with spatial differences in effective stress and displacement. Together with the observed upslope expansion of field deformation, these results link the zones into a continuous process: hydraulic disturbance first deforms Zone I, the resulting loss of support draws Zone II forward, and Zone II transmits traction to Zone III. Model masses 1–3 are material and structural units within the strongly deformed area and are defined differently from field Zones I–III. The model thus supports an interpretation of deformation transfer between the field zones rather than a one-to-one correspondence between model sensors and field zones.

Zone I is particularly sensitive to drawdown because it straddles the reservoir fluctuation zone. External water pressure decreases as the reservoir falls, whereas groundwater discharge within the slope lags behind. The delayed pore pressure peaks in the physical test and bending of the front-edge phreatic surface during numerical drawdown both indicate a difference in the timing of internal and external head adjustment. Outward seepage and the loss of external water support act together at the front, promoting movement toward the free face. Repeated immersion softens the soil, while fine-particle migration during drawdown damages its structure and reduces shear resistance. Material permeability tests show that the hydraulic conductivity of the phyllite-dominated gravelly soil in sliding mass 2 is lower than that of masses 1 and 3, demonstrating differences in permeability between masses. Together with the pore pressure lag observed in the physical model, this indicates that delayed local drainage helps maintain the head difference between the slope and reservoir during drawdown. These hydraulic and material effects are concentrated at the front and influence the upper masses through reduced support. Zone I is therefore both the direct recipient of the drawdown disturbance and the starting point for upslope transfer of traction-driven deformation; its sensitivity reflects its position, drainage conditions and supporting role within the multi-mass slope.

Comparison with typical reservoir-bank landslides and previous model tests

Studies of the Baishuihe landslide in the Three Gorges Reservoir identify the combined influence of reservoir fluctuations and rainfall, with water level changes playing an important role (Li et al. 2017). Similar reservoir-triggered slope failures have also been reported in the Xiluodu Reservoir area (Tang et al. 2022; Zheng et al. 2021). Ni et al. (2013) examined groundwater and stability evolution in Huangtupo riverside slump-mass No. I using a model with two sliding zones. Linbang likewise reflects the joint control of hydraulic boundary changes and internal structure: drawdown produces a head difference between the slope and reservoir, while the response of individual masses and sliding zones affects the extent of deformation. Its drawdown sensitivity thus shares a hydraulic basis with these reservoir-bank landslides, and its progressive deformation also needs to be understood in the context of a composite slope structure.

A specific feature of Linbang is that major deformation begins in the submerged front and is transferred upslope through the supporting relationships between sliding masses. By linking lower-slope earth pressure changes, the J3–J2–J1 displacement sequence, opening of mass boundaries and pore pressure lag, this study provides process evidence for the development of traction-driven retrogressive deformation from a local disturbance. Pan et al. (2016) demonstrated graded, blockwise sliding in centrifuge tests, while Liu et al. (2020) investigated progressive deterioration of a pile-reinforced landslide under long-term reservoir cycles. Building on these findings, the present study emphasizes interactions between the submerged mass and adjacent masses, rather than treating retrogression or the adverse effect of drawdown itself as a new failure mode. Compared with these cases, the more distinctive feature of the Linbang landslide is the spatial coincidence between the outcrop of the weak zone and the reservoir

water level fluctuation zone: the position of the controlling slip zone itself determines where the hydraulic disturbance acts and where the traction transfer starts.

The hydraulic responses also differ between cases. The Baishuihe study considered the joint effects of rainfall and reservoir level (Li et al. 2017), whereas Linbang displacement was more closely associated with drawdown and rainfall had a secondary influence during the monitoring period. This difference should be interpreted in relation to rainfall conditions, drainage pathways and the location of deformation in each case. The two sliding zones at Huangtupo are also not directly equivalent to the material layering and mass boundaries represented in the Linbang model. Similar hydraulic processes can therefore produce different patterns of deformation and transfer in different slope structures; the sensitivity or thresholds of a single case should not be generalized without considering these differences.

Implications for monitoring and stabilization in mountain reservoirs

Monitoring of ancient multi-mass landslide deposits in mountain reservoirs should extend from the front-edge fluctuation zone to the boundaries of the upper masses. In Zone I, reservoir level, internal pore pressure or groundwater level, and displacement should be observed together to identify head differences and acceleration during drawdown. In Zone II, boundary cracks and relative displacement can indicate whether front-edge deformation is being transmitted upslope. In Zone III, rear cracks, settlement and subsurface displacement can reveal expansion of the passively dragged area. Considering the response sequence across zones provides more information on progressive deformation than cumulative displacement at a single point. In the light of the spatial analysis presented above, the outcrop of the strongly weathered phyllite gravelly soil weak zone and a certain range above and below the normal storage level, together with its boundary with the overlying masses, are the parts where hydraulic disturbance is most concentrated and material degradation most persistent, and they should be treated as priority zones for monitoring and for drainage and filter-protected treatment.

Monitoring should cover the full drawdown period and continue after the reservoir level stabilizes to capture delayed drainage and deformation. Observations should be more frequent during initial impoundment and subsequent rapid drawdown, while rainfall and shallow water content should continue to be recorded to identify superimposed rainfall effects. Lower average displacement rates in later cycles may reflect adjustment of the slope response, but cracks, pore pressure and particle loss must also be considered before assessing its long-term stability.

Stabilization should address front-edge restraint, drainage and protection against seepage erosion together. Drainage at the front and along soil–rock contacts should incorporate filters to limit fine-particle loss. Retaining or anchoring measures at the front should account for loads from the upper masses and the potential sliding surfaces, including force transfer between adjacent masses. Reservoir operation and treatment options should be assessed using measured groundwater recession to evaluate the effects of different drawdown rates. The present findings help identify priority locations and processes; safe drawdown rates, drain spacing and reinforcement capacity require site-specific design calculations.

Limitations and future work

The physical model simplifies the geology of the strongly deformed area and the reservoir history because of limits imposed by box dimensions, material preparation and test duration. It cannot fully reproduce the three-dimensional field geometry or lateral constraints, and model sensors do not correspond one-to-one with field monitoring points. Model–field comparison therefore focuses on deformation stages, drawdown response and the sequence of propagation from front to rear. Model displacement magnitudes and the exact timing of stepwise movement cannot be transferred directly to the field. In addition, the slip-surface horizons were determined mainly from the weak intercalation and its upper and lower interfaces revealed by the engineering geological survey and boreholes, while the currently active slip surface was identified from the displacement-depth curves of the six borehole inclinometers; because the casings failed within 7-15 days, the effective data cover only May-June 2017, and the stability of the slip-surface position over longer periods still requires further constraint from deep displacement monitoring.

The numerical analysis assigns uniform properties within each soil type and does not account for spatial differences in gradation, density, strength and permeability within that type. In the field, crack growth and fine-particle loss may also change the soil structure and cause strength and permeability to evolve over successive reservoir cycles. The groundwater boundary was set using engineering analogy and experience and requires further evaluation against field groundwater records. The rainfall scenarios cover only selected intensities and durations and cannot represent all combinations of rainfall and drawdown. These simplifications may affect calculated local pore pressures, deformation concentrations and stability coefficients.

Future work could combine groundwater level, pore pressure and subsurface displacement monitoring across the deformation zones to examine the timing of propagation from the front toward the middle and rear. Sampling at different depths and laboratory testing could establish spatial differences in soil properties. Controlled tests with

different drawdown rates, rainfall durations and loading sequences would further clarify their combined effects. Numerical models could incorporate spatial variability and changes in strength and permeability caused by crack growth and particle loss to investigate the conditions under which local deformation spreads over a larger area.

Conclusions

Based on the similarity theory, the strongly deformed area of the Linbang landslide was generalized, and a large-scale indoor physical model test was conducted to analyze the dynamic response of the slope under actual reservoir water level fluctuations. Comparison of the test observations with field monitoring results shows that the displacement time-series characteristics and deformation rate laws recorded in the model test are significantly correlated with the field monitoring data, and their deformation trends in key stages are highly consistent. The test effectively reveals the mechanical mechanism of progressive failure of the landslide under the coupling of reservoir water level fluctuations and rainfall, and successfully reproduces the whole evolution process. The main conclusions are as follows:

(1) In terms of the mechanical mechanism, the failure mode of the strongly deformed area of the Linbang landslide is progressive retrogressive, and the deformation evolution is divided into three stages: (a) the acceleration stage caused by softening and settlement of the submerged slope during the initial water level rise; (b) the stepwise deformation stage during water level decline, when the outward seepage force formed by the hydraulic gradient is superimposed with pore water pressure to reduce stability, and the phyllite-dominated gravelly soil generates larger excess pore water pressure, aggravating the deformation; and (c) the deceleration stage during water level rise, when the reversed hydraulic gradient forms an inward seepage force that offsets the sliding force of the slope self-weight and, together with the external hydrostatic pressure, offsets part of the sliding component and slows deformation; during this stage the increase in pore water pressure reduces the effective stress, and the net effect depends on the competition among the seepage force, the hydrostatic pressure and strength softening.

(2) The initial impoundment has the most significant influence on the deformation and stability of the bank slope, when the slope is in the acceleration stage. In subsequent water level cycles, the deformation degree and rate decrease, indicating that the bank slope continuously adjusts its own stress field during periodic water level changes and reduces its sensitivity to reservoir water fluctuations, showing self-adaptability.

(3) The physical model test shows that the failure of the strongly deformed area extends gradually from the front edge to the rear, with obvious tension cracks and multi-level steps finally appearing at the rear of the model. From the perspective of the whole slope, the tension cracks at the rear of the strongly deformed area provide sliding space for the upper part of the landslide, showing progressive failure from the strongly deformed area at the front upward; the overall deformation and failure mode of the Linbang landslide is therefore progressive retrogressive.

(4) The lower outcrop of the strongly weathered phyllite gravelly soil weak zone coincides vertically with the reservoir water level fluctuation zone. This coupling of position and material determines how reservoir water acts on the slope: the layer is immersed for the longest time and has the strongest water retention capacity, and its measured mean permeability coefficient is only 0.001226 cm/s, about 1/26 and 1/29 of that of the adjacent gravelly soils, so that the head difference between the slope and the reservoir accumulates and is released mainly within this layer. The combined disadvantage of position and material provides the hydraulic basis for the differential deformation of the masses.

(5) The action of reservoir water is transmitted upwards through a process of deformation of the submerged part, differential displacement at the boundaries and traction of the upper masses: the submerged weak zone responds earlier than the upper masses and, through immersion-induced softening and settlement, weakens the support of the upper masses, which then move towards the free face, so that cracks open at the boundaries and tension cracks and multi-level steps appear at the rear and the slope as a whole fails in a retrogressive manner. Accordingly, the outcrop of the weak zone and a certain range above and below it, together with its boundary with the overlying masses, should be treated as priority zones for deformation monitoring, drainage and filter-protected treatment.

Data availability: The data presented in this study are available on request from the corresponding author.

Author contributions: Conceptualization, M.X. and J.L.; methodology, J.L.; validation, C.L. and M.X.; investigation, J.L., S.J. and C.H.; data curation, J.H.; writing—original draft preparation, J.L.; writing—review and editing, M.X. All authors have read and agreed to the published version of the manuscript.

References

Biniyaz A, Azmoon B, Liu Z (2022) Coupled transient saturated-unsaturated seepage and limit equilibrium analysis for slopes: influence of rapid water level changes. Acta Geotechnica 17(6):2139-2156. https://doi.org/10.1007/s11440-021-01359-7

Chen Y, Xu J, Peng S, Zhang Q, Chen C (2023) Space-time evolution law of progressive failure area and mechanical behaviour of rock under different seepage conditions. Engineering Geology 312:106926. https://doi.org/10.1016/j.enggeo.2022.106926

Corbyn JA (1982) Failure of a partially submerged rock slope with particular reference to the Vajont rock slide. International Journal of Rock Mechanics and Mining Sciences & Geomechanics Abstracts 19(2):99-102. https://doi.org/10.1016/0148-9062(82)91635-7

Corominas J, Moya J, Ledesma A, Lloret A, Gili JA (2005) Prediction of ground displacements and velocities from groundwater level changes at the Vallcebre landslide (Eastern Pyrenees, Spain). Landslides 2(2):83-96. https://doi.org/10.1007/s10346-005-0049-1

Du F, Xu M, Xiao X et al (2018) Physical simulation modeling for stability analysis of reservoir landslide in gently underdip slopes: a case study of Xiangjiaping landslide. Journal of Engineering Geology 26(3):694-702. https://doi.org/10.13544/j.cnki.jeg.2017-175 (in Chinese)

Fujita H (1977) Influence of water level fluctuations in a reservoir on slope stability. Bulletin of the International Association of Engineering Geology 16(1):170-173. https://doi.org/10.1007/BF02591474

Griffiths DV, Lane PA (1999) Slope stability analysis by finite elements. Géotechnique 49(3):387-403. https://doi.org/10.1680/geot.1999.49.3.387

Huang QX, Wang JL, Xue X (2016) Interpreting the influence of rainfall and reservoir infilling on a landslide. Landslides 13(5):1139-1149. https://doi.org/10.1007/s10346-015-0644-8

Huang RQ (2007) Large-scale landslides and their mechanisms in China since the 20th century. Chinese Journal of Rock Mechanics and Engineering 26(3):433-454 (in Chinese)

Iqbal J, Tu X, Gao W (2019) The impact of reservoir fluctuations on reactivated large landslides: a case study. Geofluids 2019:2374236. https://doi.org/10.1155/2019/2374236

Jian WX, Xu Q, Yang HF, Wang FW (2014) Mechanism and failure process of Qianjiangping landslide in the Three Gorges Reservoir, China. Environmental Earth Sciences 72(8):2999-3013. https://doi.org/10.1007/s12665-014-3205-x

Kafle L, Xu WJ, Zeng SY, Nagel T (2022) A numerical investigation of slope stability influenced by the combined effects of reservoir water level fluctuations and precipitation: a case study of the Bianjiazhai landslide in China. Engineering Geology 297:106508. https://doi.org/10.1016/j.enggeo.2021.106508

Li DC, Wang ZJ, Shao JP et al (2017) Analysis on deformation mechanism of Baishui River landslide under rainfall and reservoir water level coupling. Journal of China Three Gorges University (Natural Sciences) 39(4):46-50 (in Chinese)

Li SL, Tang MG, Xu Q et al (2020) Centrifugal model tests on buoyancy-induced weight-loss landslides influenced by rising reservoir water level. Journal of Northeastern University (Natural Science) 41(5):616-622, 634. https://doi.org/10.12068/j.issn.1005-3026.2020.05.002 (in Chinese)

Li SL (2021) Study on the reactivation characteristic and deformation self-adaptive of landslides in the Three Gorges Reservoir area. Dissertation, Chengdu University of Technology, Chengdu (in Chinese)

Liu DZ, Hu XL, Zhou C, Xu C, He CC, Zhang H, Wang Q (2020) Deformation mechanisms and evolution of a pile-reinforced landslide under long-term reservoir operation. Engineering Geology 275:105747. https://doi.org/10.1016/j.enggeo.2020.105747

Mao JZ, Guo J, Fu Y, Zhang WP, Ding YN (2020) Effects of rapid water-level fluctuations on the stability of an unsaturated reservoir bank slope. Advances in Civil Engineering 2020:2360947. https://doi.org/10.1155/2020/2360947

Ni WD, Tang HM, Hu XL et al (2013) Research on deformation and stability evolution law of Huangtupo riverside slump-mass No. I. Rock and Soil Mechanics 34(10):2961-2970 (in Chinese)

Pan HS, Li TB, Xu BY et al (2016) Centrifugal model tests on large-scale landslide with broken-line slip surface under rainfall. Chinese Journal of Rock Mechanics and Engineering 38(4):696-704 (in Chinese)

Schuster RL (1979) Reservoir-induced landslides. Bulletin of the International Association of Engineering Geology 20(1):8-15. https://doi.org/10.1007/BF02591233

Shen J, Gao Y, Wen L, Jin X (2018) Deformation response regularity of Liujiaba landslide under fluctuating reservoir water level condition. Natural Hazards 94(1):151-166. https://doi.org/10.1007/s11069-018-3378-9

Tang FJ, Qi SW, Guo SF et al (2022) Spatio-temporal distribution pattern and susceptibility of reservoir-induced landslides in the Xiluodu Hydropower Station area. Journal of Engineering Geology 30(3):609-620 (in Chinese)

Tang JF, Tang XM, Zeng XN et al (2018) Deformation characteristics and stability analysis of deposit slope after initial impoundment. Journal of Jilin University (Earth Science Edition) 48(5):1546-1555 (in Chinese)

Xia Z, Song K, Yi Q et al (2020) Influencing factor analysis of large rock reservoir landslide during reactivation deformation process. Water Resources and Power 38(8):114-117, 113 (in Chinese)

Xiao SR, Liu DF, Hu ZY et al (2010) Geomechanical model experiment on Qianjiangping landslide in the Three Gorges Reservoir area. Chinese Journal of Rock Mechanics and Engineering 29(5):1023-1030 (in Chinese)

Yang H, Tang MG, Xu Q et al (2021) Research of statistical characteristics of deformation of landslides in the Three Gorges Reservoir area of the Yangtze River. Journal of Catastrophology 36(2):37-42 (in Chinese)

Yu SY, Ren XH, Zhang JX, Wang HJ, Wang JL, Zhu WW (2020) Seepage, deformation, and stability analysis of sandy and clay slopes with different permeability anisotropy characteristics affected by reservoir water level fluctuations. Water 12(1):201. https://doi.org/10.3390/w12010201

Zhao JJ, Pan HN, He JX et al (2025) Research on formation mechanism of weak base landslide in tectonic melange zone: case of Baige landslide. Yangtze River 56(9):20-32 (in Chinese)

Zheng HY, Cui HB, Li RJ et al (2021) Analysis on the process and genesis of Huangping landslide in the reservoir area of Xiluodu Hydropower Station. Yangtze River 52(S1):93-95 (in Chinese)

Zou ZX, Tang HM, Criss RE, Hu XL, Xiong CR, Wu Q, Yuan Y (2021) A model for interpreting the deformation mechanism of reservoir landslides in the Three Gorges Reservoir area, China. Natural Hazards and Earth System Sciences 21(2):517-532. https://doi.org/10.5194/nhess-21-517-2021

Supplementary Files

This is a list of supplementary files associated with this preprint. Click to download.

- ElectronicSupplementaryMaterialEESroute2.docx